https://doi.org/10.5194/egusphere-2026-4229
Preprint. Discussion started: 28 July 2026

Introduction of prognostic aerosols in the P3 microphysics scheme: Simulation of layered Arctic mixed-phase clouds

Mélissa Cholette[1], Caroline Jouan[2], Hugh Morrison[3], Jason A. Milbrandt[1], Zhipeng Qu[1], Zane Dedekind[1], Alexei Korolev[1], Zen Mariani[1]

[1]Meteorological Research Division, Environment and Climate Change Canada, Toronto, Canada
[2]Center for International Climate Research, Oslo, Norway
[3]NSF National Center for Atmospheric Research, Boulder, Colorado, USA

Correspondence to: Mélissa Cholette (melissa.cholette@ec.gc.ca)

Abstract. This study presents the implementation of prognostic aerosols within the Predicted Particle Properties (P3) microphysics scheme to improve the physical consistency of aerosol–cloud–precipitation interactions. Two new prognostic number mixing ratio variables representing "water-friendly" (CCN) and "ice-friendly" (INP) aerosols are added. Aerosols then evolve dynamically and interact with hydrometeors via nucleation, scavenging, evaporation, and sublimation. The impacts of the modified scheme are investigated using convection-permitting (1-km horizontal grid spacing) simulations of an Arctic mixed-phase cloud case observed on 19–20 January 2026 near Inuvik, Canada. Simulations are compared against "in situ" observations, ground-based radar measurements, and retrievals from the EarthCARE satellite.

Results show that the inclusion of prognostic aerosols significantly affects cloud microphysical properties and phase partitioning. The prognostic aerosol simulation produces systematically fewer but larger ice particles, leading to increased reflectivity and enhanced riming. It also results in higher liquid water content and lower ice water content compared to the simulation without prognostic aerosols, thereby favoring the persistence of supercooled liquid layers and improving agreement with retrievals. Sensitivity experiments demonstrate that the choice of ice nucleation parameterization plays a dominant role in controlling the cloud phase. Aerosol-dependent formulations produce lower ice crystal concentrations and more persistent liquid water than the original temperature-dependent scheme, thereby enhancing mixed-phase cloud occurrence. The new prognostic aerosol framework improves the representation of aerosol-cloud indirect effects in P3 and provides a pathway toward more accurate simulations of clouds and precipitation, which are critical for radiative balance and weather prediction in polar regions and elsewhere.

1 Introduction

Aerosol particles play a key role in cloud formation and precipitation processes by acting as cloud condensation nuclei (CCNs) and ice nucleating particles (INPs) (e.g., Hudson, 1993; Kanji et al., 2017). Aerosols influence Earth's radiative balance through three main processes: directly, by reflecting solar radiation back to space in the case of scattering aerosols; indirectly, by modifying cloud properties and precipitation processes (e.g., cloud lifetime, phase partitioning, and precipitation

https://doi.org/10.5194/egusphere-2026-4229
Preprint. Discussion started: 28 July 2026

efficiency); and semi-directly, by heating the atmosphere in the case of absorbing aerosols and thereby altering the thermodynamic processes that govern cloud formation (e.g., Fan et al., 2016; Lohmann, 2006; Ramanathan et al., 2001; Rosenfeld, 2006; Rosenfeld et al., 2014; Yu et al., 2024). Aerosol-cloud-precipitation (ACP) interactions are complex, as multiple processes occur simultaneously. For example, an increase in CCN leads to a higher cloud droplet number concentration and smaller droplet sizes, which suppresses precipitation and can extend cloud lifetime (e.g., Albrecht, 1989).

Over the past decades, based primarily on satellite observations and "in situ" measurements, advancements in the development and understanding of ACP interactions in the Earth's climate system have been made using, for example, global and regional climate models (e.g., Collins et al., 2017; Fan et al., 2018; Lamarque et al., 2013; Li et al., 2019; Rosenfeld et al., 2008; Wang et al., 2018; Zhao et al., 2018). This has led to improvements in numerical weather prediction (NWP) systems at global and regional scales, such as the developments of (1) bulk microphysics schemes that explicitly account for the aerosol effects (Jian et al., 2026; Thompson and Eidhammer, 2014), and (2) atmospheric chemistry modules coupled to NWP models (e.g., Grell et al., 2005; Moran et al., 2025).

Operational NWP systems treat aerosols with varying levels of complexity depending on the model resolution and the forecasting priorities. Meteorological centers such as the European Centre for Medium-Range Weather Forecasts (ECMWF), the National Oceanic and Atmospheric Administration (NOAA), the UK Met Office, the Japan Meteorological Agency (JMA), the China Meteorological Administration (CMA), and Environment and Climate Change Canada (ECCC) typically include either prognostic or semi-prognostic aerosol schemes within global and/or regional NWP systems, such as the Integrated Forecast System (IFS; Rémy et al., 2019), the Global Forecasting System (GFS; Jiang et al., 2017), the Unified Model-UKCA (Ghosh et al., 2025; Walters et al., 2019), and the Regional Air Quality Deterministic Prediction System (RAQDPS; Moran et al., 2025). In these systems, aerosols (e.g., dust, sea salt, sulfate, black carbon) are often assimilated from satellite products, and then transported and directly accounted for in radiative transfer calculations. However, the indirect effects of aerosols on cloud microphysics and precipitation processes are mostly simplified and/or only partially represented. For example, the current (at the time of writing) RAQDPS uses the Sundqvist large-scale condensation scheme (Sundqvist et al., 1989) to predict clouds and precipitation; this scheme includes only a single prognostic cloud variable (i.e., the mass of non-sedimenting total condensate) and does not separate the liquid and the ice phases; thus, it does not predict cloud number concentration nor does it include aerosol activation or droplet nucleation parameterizations.

Despite advances in modelling ACP interactions, such interactions remain a major source of uncertainty in atmospheric numerical modelling, particularly at high-resolution NWP and for high-impact weather events such as deep convection events (e.g., Khain et al., 2005; Morrison et al., 2020; Papaevangelou et al., 2025). In contrast to large-scale models, high-resolution or convection-permitting NWP models use bulk microphysics parameterizations because they are computationally efficient and able to represent a wide range of cloud processes across scales (e.g., Morrison et al., 2020). Most high-resolution NWP models still employ simplified representations of ACP interactions, however, to address this limitation, several models such as WRF-Chem (Grell et al., 2005), CMA-MESO (Jian et al., 2026; Zhou et al., 2016), and the HRRR (James et al., 2022), have

https://doi.org/10.5194/egusphere-2026-4229
Preprint. Discussion started: 28 July 2026

implemented fully coupled ACP interactions that account for aerosol activation and cloud and ice nucleation within their bulk microphysics schemes.

Among bulk microphysics schemes, the Predicted Particle Properties (P3; Morrison and Milbrandt, 2015; hereafter MM15) scheme offers a flexible, physically based framework for representing clouds and precipitation, with a prognostic treatment of several bulk hydrometeor properties (e.g., Cholette et al., 2019, 2023; Milbrandt and Morrison, 2016). P3 has been used in many atmospheric models operating at different scales including global-scale (e.g., ECHAM6; Dietlicher et al., (2018), E3SM; Wang et al., (2021)), mesoscale (e.g., MPAS, FV3, and WRF; MM15; Morrison et al., (2015)), and cloud-resolving scale such as SAM and CM1 (e.g., Dengate et al., (2025), ICON; Seifert and Siewert, (2024) and VVM; e.g., Kuo et al., (2026)). P3 is used operationally in ECCC's GEM-based High Resolution Deterministic Prediction Systems (HRDPS; Milbrandt et al., 2016) and Canadian Arctic Prediction System (CAPS; Casati et al., 2023). Like many other bulk microphysics schemes, the existing P3 scheme uses a prescribed CCN concentration that is fixed in time and space and neglects INP effects entirely, thereby limiting the physical consistency of ACP interactions.

The present study aims to improve the representation of ACP interactions in P3 by introducing two new prognostic variables: the "water-friendly" and "ice-friendly" aerosol number mixing ratios. This approach enables a more physically coherent representation of some microphysical processes such as activation. The focus is on the simulations of an Arctic mixed-phase clouds (MPCs) case because their phase partitioning, ice production, lifetime, and radiative effects are strongly controlled by CCNs and INPs (e.g., de Boer et al., 2011; Korolev and Milbrandt, 2022; Paukert and Hoose, 2014; Ross and Lasher-Trapp, 2025; Solomon et al., 2018; Xie et al., 2013). Therefore, Arctic MPCs provide a useful testbed for aerosol-cloud coupling. These clouds can persist for hours to days over a wide range of thermodynamic conditions and varying horizontal and vertical extents, while microphysical processes such as heterogeneous ice nucleation and the Wegener-Bergeron-Findeisen process strongly regulate their evolution (e.g., Korolev, 2007a; Korolev and Milbrandt, 2022; Korolev, 2008; Morrison et al., 2012).

Accurately forecasting supercooled liquid layers embedded in or above ice-phase clouds is critical for Earth's radiative budget and aircraft icing forecasts (Cober et al., 2001; Cober and Isaac, 2012; Kanji et al., 2017; Rasmussen et al., 2006). However, Arctic MPCs remain challenging to simulate because models often overproduce ice at the expense of supercooled liquid water and inadequately represent aerosol-dependent nucleation, riming, aggregation, and boundary-layer dynamics (e.g., Forbes and Ahlgrimm, 2014). Several studies have highlighted the importance of INP representation in the simulations of Arctic MPCs in climate models, large-eddy simulation (LES) or using bulk microphysics schemes in NWP models (Burrows et al., 2022; Fu and Xue, 2017; Gjelsvik et al., 2025; Glassmeier et al., 2017; Murray et al., 2012; Norgren et al., 2018; Paukert and Hoose, 2014; Sauerland et al., 2024; Schäfer et al., 2025; Shi et al., 2022; Solomon et al., 2018; Sotiropoulou et al., 2021; Tan et al., 2023; Zhao and Liu, 2022). For example, Morrison and Pinto, (2005, 2006) concluded that INP representation strongly controls condensate partitioning between liquid and ice in Arctic mixed-phase clouds as increasing INP concentrations enhanced glaciation and reduced supercooled liquid water persistence.

https://doi.org/10.5194/egusphere-2026-4229
Preprint. Discussion started: 28 July 2026

The remainder of this paper is organized as follows: Section 2 describes the P3 scheme and the implementation of prognostic aerosols. Section 3 presents the experimental design, including the NWP model configuration, the case study, and the analysis method. Section 4 discusses the results, focusing on the impacts of prognostic aerosols within P3 and the sensitivity to ice nucleation parameterizations. Section 5 presents conclusions and outlines directions for future work.

2 The P3 scheme and implementation of prognostic aerosols

2.1 The P3 scheme overview

The P3 microphysics scheme used in this study is the latest version, designated as v6.0. Version 6.0 is based on v5.5, which is described in Appendix A, and includes developments associated with the implementation of prognostic aerosols in P3. The implementation of prognostic aerosols follows Thompson and Eidhammer (2014), as described in Appendix B, with some modifications explained below. The prognostic aerosol option can be enabled or disabled at runtime. The scheme reverts to the original v5.5 configuration when prognostic aerosols are not used.

The baseline P3 v5.5 has a double-moment particle size distribution (PSD) representation for cloud droplets and rain drops (MM15), and a three-moment PSD for ice/mixed-phase particles (Cholette et al., 2023; Milbrandt et al., 2021; Morrison et al., 2025). Cloud, rain and ice PSDs are represented by gamma functions. The representation of the ice phase in P3 does not assume fixed properties of the traditional bulk approach using predefined categories such as hail, graupel, snow and cloud ice. Instead, bulk ice is allowed to evolve continuously over different growth processes (deposition and riming). Particles in each freely-evolving generic ice category (Milbrandt and Morrison, 2016) are described by a set of bulk particle properties, such as mean fall speed, mass, density, rime and liquid mass fractions, allowing a wide range of properties depending on the microphysical evolution of hydrometeors. In this study, the single ice-phase category configuration is used as it is the configuration closer to what is used operationally in the km-scale NWP systems at ECCC.

P3 prognoses four mixing ratios (per kg of dry air) for the liquid phases: q_c [kg kg^{-1}] for cloud droplet mass, N_c [# kg^{-1}] for cloud droplet number, q_r [kg kg^{-1}] for rain mass and N_r [# kg^{-1}] for rain number, and up to six prognostic variables for each ice category: total ice number ($N_{i,tot}$, in # kg^{-1}), total ice mass ($q_{i,tot}$, in kg kg^{-1}), rime mass ($q_{i,rim}$, in kg kg^{-1}), rime volume ($B_{i,rim}$, in m^3 kg^{-1}), liquid on ice mass ($q_{i,liq}$, in kg kg^{-1}) and the 6th moment ($Z_{i,tot}$, in m^6 kg^{-1}) of the PSD. The last two prognostic variables, although optional in the code, are used in this study. They represent the inclusion of mixed-phase particles within the ice category (Cholette et al., 2019) and the three-moment representation of the ice PSD (Morrison et al., 2025), respectively.

The total ice mass mixing ratio given by Eq. (1) is the sum of $q_{i,dep}$ (the ice mass mixing ratio from vapor diffusion grow), $q_{i,rim}$, and $q_{i,liq}$. The quantity $q_{i,ice}$ is the total dry (solid) ice mass mixing ratio (i.e., $q_{i,dep} + q_{i,rim}$). All variables are defined in Appendix C. The bulk liquid and rime mass fractions are $F_{i,liq} = q_{i,liq}/q_{i,tot}$ and $F_{i,rim} = q_{i,rim}/q_{i,ice}$, respectively.

https://doi.org/10.5194/egusphere-2026-4229
Preprint. Discussion started: 28 July 2026

The descriptions of the P3 scheme, including detailed microphysical processes, particle size functions, and prognostic equations, are provided in MM15, Cholette et al. (2019, 2023), Milbrandt et al. (2021), Morrison et al. (2025).

$$q_{i,tot} = q_{i,dep} + q_{i,rim} + q_{i,liq} = q_{i,ice} + q_{i,liq} \tag{1}$$

2.2 Implementation of prognostic aerosols in P3

Two new prognostic variables are added in the code: $N_{a,w}$ (Eq. 2) and $N_{a,i}$ (Eq. 3), which represent the "water-friendly" and "ice-friendly" aerosols number mixing ratios, respectively.

$$\frac{\partial N_{a,w}}{\partial t} = N_{c,evp} + N_{r,evp} + N_{a,w\,sfc\_emission} - N_{c,nuc} - N_{aw,hom} - N_{r,wsca} - N_{i,wsca} \tag{2}$$

$$\frac{\partial N_{a,i}}{\partial t} = N_{i,sub} + N_{l,evp} + N_{a,i\ sfc\_emission} - N_{i,nuc} - N_{r,isca} - N_{i,isca} \tag{3}$$

The right-hand side of these equations are the microphysical source/sink terms. The full time tendencies of both aerosol variables follow the governing equation for conservation (Eq. 4) where X denotes any species mixing ratio (cloud, rain, ice, and aerosols), t is time, z is height, ρ_{air} is air density, **U** is the 3D wind vector**,** V_X is the weighted fall speed of X, $\Delta^*(X)$ is the subgrid-scale operator and S_X are the various microphysical process rates, described in Appendix B.

$$\frac{\partial X}{\partial t} = -\mathbf{U}\cdot\nabla X + \frac{1}{\rho_{air}}\frac{\partial(\rho_{air}V_X\,X)}{\partial z} + \Delta^*(X) + S_X \tag{4}$$

In Eqs. (2–3), $N_{c,nuc}$ is cloud nucleation, $N_{c,evp}$ and $N_{r.evp}$ are cloud and rain evaporation, $N_{i,sub}$ is ice sublimation, $N_{l,evp}$ is liquid evaporation of mixed-phase particles, $N_{i,nuc}$ is ice nucleation, $N_{r,wsca}$ is rain collecting $N_{a,w}$, $N_{i,wsca}$ is ice collecting $N_{a,w}$, $N_{r,isca}$ is rain collecting $N_{a,i}$, $N_{i,isca}$ is ice collecting $N_{a,i}$, $N_{aw,hom}$ is the freezing of aqueous aerosols, and $N_{a,w\,sfc\_emission}$ and $N_{a,i\,sfc\_emission}$ are surface emissions of water-friendly and ice-friendly aerosols, respectively.

After initialization using linear interpolation to the model start date from the monthly averages derived from multiyear (2001–2007) global model simulations with 0.5° longitude and 1.25° latitude resolution (Colarco et al., 2010), $N_{a,w}$ and $N_{a,i}$ evolve microphysically following Eqs. (2) and (3), respectively, and near-surface emissions at every time step are included by relaxing the values back toward the climatology (Appendix B1). It is found that values at the lowest model level increased too rapidly when the surface emissions were treated as in Thompson and Eidhammer (2014), therefore the surface emission described in Appendix B1 is used instead. Although in this study the surface emissions did not strongly affect the solution because of the short simulation period (24 h) and relatively weak vertical motions (< 1 m s^{-1}), these empirically constrained emissions are important to ensure a surface source for $N_{a,w}$ and $N_{a,i}$.

Cloud nucleation $N_{c,nuc}$ (Appendix B2) is modified to account for $N_{a,w}$ compared with a constant value in baseline P3. The parameterization of Khvorostyanov and Curry (2005) is used in baseline P3 and based on water supersaturation and a fixed CCN concentration of 300 × 10^6 # kg^{-1}. The parameterization of Abdul-Razzak and Ghan (2000), based on the vertical motion which includes resolved and subgrid-scale components (described in Appendix B2), is used in the prognostic aerosol configuration. Since vertical motion is weak overall in the context of this study, both cloud nucleation parameterizations, with either a constant or varying $N_{a,w}$, give similar results (not shown).

https://doi.org/10.5194/egusphere-2026-4229
Preprint. Discussion started: 28 July 2026

The ice nucleation formulation is also modified with prognostic aerosols and no longer uses the P3's original temperature-dependent Cooper (1986; hereafter C86) formulation in the baseline P3 (Appendix B3). With prognostic aerosols, the DeMott et al. (2010; hereafter DM10) formulation, which accounts for the prognostic $N_{a,i}$, is used (Appendix B3). A third ice nucleation parameterization from Tobo et al. (2013; hereafter T13) is also implemented in P3 with prognostic aerosols and is evaluated in this study (Appendix B3).

Vapor transfer terms $N_{r,evp}$, $N_{i,sub}$ and $N_{l,evp}$ (Appendix B4 and B5) are computed as in the baseline P3 and consist of source terms for the aerosol number mixing ratios (Eqs. 2–3). The cloud droplet number mixing ratio tendency due to cloud evaporation ($N_{c,evp}$; Appendix B5) is a source term for $N_{a,w}$ and a new sink term for N_c in the prognostic aerosol configuration; that is, $N_{c,evp}$ is not included in the baseline P3. In the experimental set-up of this study, the impact of including $N_{c,evp}$ in the baseline P3 is small (not shown) but impacts on simulations of different weather regimes and in different numerical models remain to be investigated. Finally, homogeneous freezing of $N_{a,w}$ ($N_{aw,hom}$; Appendix B8) and the four collection terms between aerosols and hydrometeors ($N_{r,wsca}$, $N_{i,wsca}$, $N_{r,isca}$ and $N_{i,isca}$; Appendix B6–B7) are sink and source terms with prognostic aerosols.

3. Experimental Design

3.1 Description of simulations

Simulations with 1 km horizontal grid spacing were performed using the nonhydrostatic configuration of the Global Environmental Multiscale model (GEM; Côté et al., 1998; Girard et al., 2014), which is the operational NWP model used in all weather prediction systems at ECCC. The GEM dynamical core solves the compressible Euler equations using an implicit treatment in time and a semi-Lagrangian advection scheme (Girard et al., 2014). The 3 km grid spacing operational Canadian Arctic Prediction System (CAPS; Casati et al., 2023) is used to provide initial and hourly lateral boundary conditions for the 1 km grid spacing simulations, whose domain is nested within the CAPS domain (Fig. 1).

The 1-km simulations were performed in the context of the Polar Night Experiment (PONEX; https://hiwr.ca/ponex/), an aircraft and surface field campaign designed to explore atmospheric physics and chemistry in the Canadian Arctic during the polar night and polar sunrise conditions. PONEX took place from 6–21 January 2026 in Inuvik, NT. The campaign objective was to conduct satellite calibration/validation experiments for two satellite missions: HAWC (Langille et al., 2025) and EarthCARE (Eisinger et al., 2024; Illingworth et al., 2015; Wehr et al., 2023) and to improve the weather representation associated with polar night conditions in ECCC NWP systems. In this context, the development and use of 1 km grid spacing simulations enable (1) enhanced CAPS performance such as increasing the number of vertical levels to better represent boundary layer inversions, which are important for low-level clouds, and (2) testing new features such as the implementation of prognostic aerosols in the P3 scheme.

https://doi.org/10.5194/egusphere-2026-4229
Preprint. Discussion started: 28 July 2026

The differences between CAPS and the 1-km simulations are the domain size, simulation period, horizontal grid spacing, time step, number of vertical levels and whether there is coupling with the sea ice and ocean components (Table 1). Physical parameterizations are the same between CAPS and the 1-km simulation for the land surface scheme (Bélair et al., 2003, 2005) and the radiative transfer (Li and Barker, 2005). CAPS uses Kain and Fritsch (1990, 1993) for the deep convection parameterization and the Kuo-Transient scheme for shallow convection whereas the 1-km simulations are convection-permitting. CAPS uses the operational version of P3 (v3.1) while the 1-km simulations use the latest version described in Sect. 2 (v6.0).

The study focuses primarily on the impacts of prognostic aerosols within P3. The 1-km control simulation uses the baseline P3 (i.e., no prognostic aerosols, one ice category, prediction of mixed-phase particles and the use of 3-moment ice PSD). This simulation is hereafter referred to as BASE. BASE is compared to the same 1-km simulation setup but including prognostic aerosols in P3: this simulation is hereafter referred to as AERO. Both BASE and AERO use the same P3 version, except that BASE does not include the two new prognostic aerosol number variables and the improved representations of their interactions with clouds whereas AERO does.

Finally, a sensitivity analysis of the choice of ice nucleation parameterizations (Table 2) is performed, given that the presence of layered mixed-phase clouds has been found to be sensitive to the selected parameterization. BASE uses the C86 ice nucleation parameterization (Eq. B11) and AERO uses the DM10 ice nucleation parameterization, which accounts for ice-friendly aerosol $N_{a,i}$ (Eq. B12). Other sensitivity simulations are as follows. Three simulations similar to BASE but using a fixed $N_{a,i}$ instead of prognostic values in the DM10 nucleation process are analysed. The assumed values are $N_{a,i}$ are 15×10^4, 15×10^5 and 15×10^6 # kg^{-1}, chosen to span the range of values present in the climatological input data. These simulations are hereafter referred to as BASE-DM10_Nai1, BASE-DM10_Nai2, and BASE-DM10_Nai3, respectively. Four additional simulations use the same configuration as AERO, but with different ice nucleation parameterizations. AERO-DM10_Nai1, AERO-DM10_Nai2 and AERO-DM10_Nai3 use DM10 but assume a constant $N_{a,i}$ of 15×10^4, 15×10^5 # kg^{-1} and 15×10^5 # kg^{-1}, respectively, AERO-C86 uses the temperature-dependent formulation of C86 instead of DM10 and AERO-T13 uses the Tobo et al. (2013) ice nucleation parameterization with prognostic $N_{a,i}$ (Eq. B13). $N_{a,i}$ is prognostic in AERO-DM10_Nai1, AERO-DM10_Nai2, AERO-C86, and AERO-T13; it is therefore advected and allowed to interact with other microphysical processes in Eq. (3), but it is held fixed during the ice nucleation calculation.

https://doi.org/10.5194/egusphere-2026-4229
Preprint. Discussion started: 28 July 2026

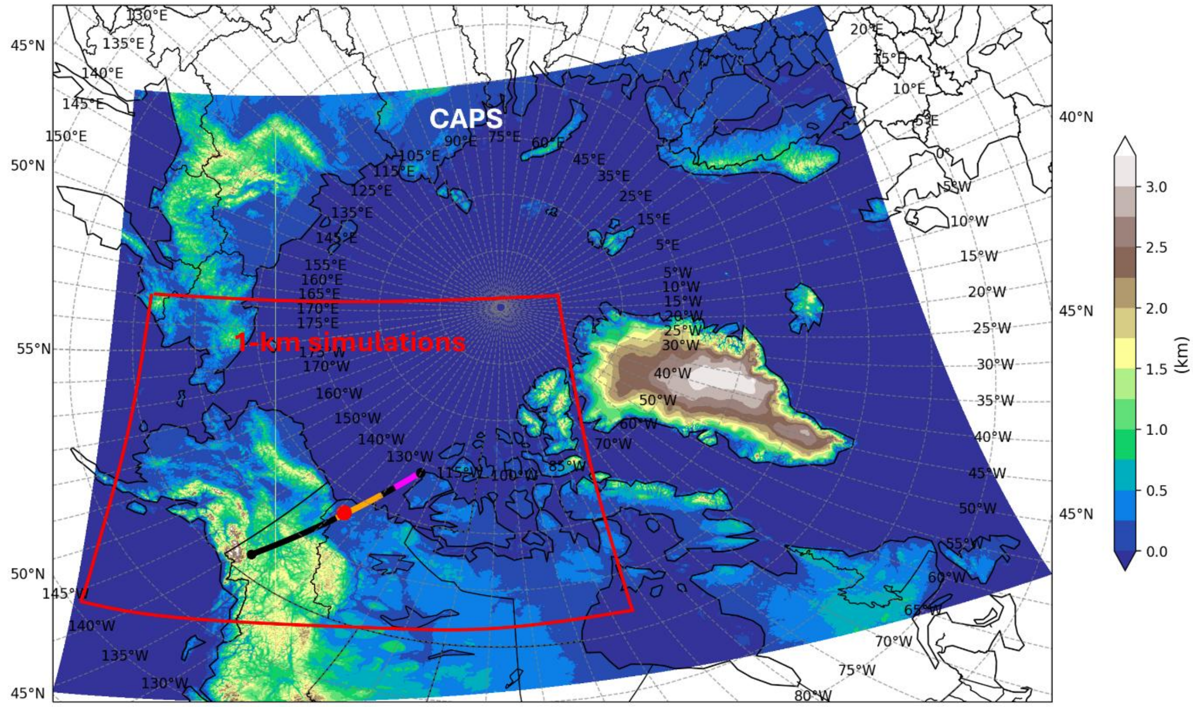

Figure 1. Elevations (colours in km) of CAPS, the domain of the 1-km grid spacing simulations (red square), the locations of Inuvik (red dot) and the EarthCARE pass (black line), with the two segments analysed in the results highlighted in orange for type A clouds and in pink for type B clouds (see section 4.1 for definitions).

https://doi.org/10.5194/egusphere-2026-4229
Preprint. Discussion started: 28 July 2026

	CAPS	1-km simulations	
		BASE	AERO
Start date	00 UTC 19 January 2026	03 UTC 19 January 2026	
Period	48 h	24 h	
Time step	60 s	30 s	
Horizontal grid spacing	0.02925° (~3 km)	0.01° (~1 km)	
# of vertical levels	62	84	
Outputs frequency	1 h	1 h	
Initial & lateral boundary conditions	Global Deterministic Prediction System (GDPS; (Buehner et al., 2015)	CAPS	
Coupled with ice/ocean	Yes	No	
Parametrization for deep and mid convection	Kain and Fritsch (1990, 1993)	None	
Parametrization for shallow convection	Kuo-Transient scheme for shallow convection (Bélair et al., 2005)	None	
Land surface scheme	Interactions between Soil, Biosphere, and Atmosphere (ISBA; (Bélair et al., 2003, 2005)		
Radiative transfer	Li-Barker correlated k-distribution method is used to compute radiative transfer every 15 min (Li and Barker, 2005)		
Microphysics	P3 (MM15) Double-moment cloud, rain and ice	P3 (Cholette et al., 2019, 2023; Morrison et al., 2025) Double-moment cloud and rain Triple-moment ice with predicted liquid fraction	
		No prognostic aerosols	With prognostic aerosols

Table 1. Configuration descriptions and differences between CAPS and the 1-km simulations.

Name	**Ice nucleation parameterization**	**Prognostic aerosols**
BASE	C86 (Eq. B11)	No
BASE-DM10_Nai1	As BASE but using DM10 with a fixed $N_{a,i}$ = 15e+4 # kg^{-1}	No
BASE-DM10_Nai2	As BASE but using DM10 with a fixed $N_{a,i}$ = 15e+5 # kg^{-1}	No
BASE-DM10_Nai3	As BASE but using DM10 with a fixed $N_{a,i}$ = 15e+6 # kg^{-1}	No
AERO	DM10 with prognostic $N_{a,i}$ (Eq. B12)	Yes
AERO-DM10_Nai1	As AERO but using a fixed $N_{a,i}$ = 15e+4 # kg^{-1}	Yes
AERO-DM10_Nai2	As AERO but using a fixed $N_{a,i}$ = 15e+5 # kg^{-1}	Yes
AERO-DM10_Nai3	As AERO but using a fixed $N_{a,i}$ = 15e+6 # kg^{-1}	Yes
AERO-C86	As AERO but using C86	Yes
AERO-T13	As AERO but using T13 with prognostic (varying) $N_{a,i}$ (Eq. B13)	Yes

Table 2. 1-km sensitivity simulations to the choice of ice nucleation parameterization.

https://doi.org/10.5194/egusphere-2026-4229
Preprint. Discussion started: 28 July 2026

3.2 Methods of analysis

The case analysed occurred on 19 January 2026 during which the EarthCARE satellite passed directly over Inuvik, Northwest Territories (NT), Canada, at around 17:00 LT corresponding to 00 UTC 20 Jan 2026 (Fig. 1). The system moved in from the Beaufort Sea and moved southeast over Inuvik between 16 UTC 19 Jan and 02 UTC 20 Jan. Precipitation accumulation was small (< 0.1 mm) at Inuvik itself but larger to the east (~5 mm), for example at Paulatuk (YPC airport).

The simulations are compared with surface and upper air "in situ" data taken at Inuvik as well as data retrieved from GOES-18 (i.e., 10.3 um radiance; NOAA) and EarthCARE satellites (Eisinger et al., 2024; Illingworth et al., 2015; Wehr et al., 2023). At Inuvik, soundings were launched every 6-h during that day and are compared to the simulations. Time series of surface meteorological fields (air temperature, relative humidity, pressure, wind speed and precipitation rate) on 19 January 2026 from a Vaisala WXT536 weather transmitter deployed at the ECCC meteorological research site in Inuvik are also analysed (Mariani et al., 2022, 2024). Co-located observations from the make (Metek) Micro Rain Radar (MRR-PRO), a K-band Doppler radar providing vertical profiles of reflectivity, are also used. The model equivalent reflectivity, cloud and ice water contents (CWC and IWC, respectively), and the cloud and ice effective radii are compared with EarthCARE retrievals (synergy: ACM-CAP, Baseline BC). Comparisons at Inuvik are made using a single grid point, closest in latitude and longitude, and, similarly, comparison along the EarthCARE track is made using grid points extracted at the closest latitude-longitude pairs at 00 UTC 20 Jan 2026.

Cloud and ice mass mixing ratios are converted to mass contents and number mixing ratios to concentrations for direct comparisons with observations. The simulated mass-weighted mean diameters of cloud and ice are computed following Eqs. (5a,b), respectively, with $\rho_{i,m}$ the mass-weighted mean density of ice (Eq. 6). The simulated effective radii of cloud and ice are given by Eqs. (7a,b), respectively.

$$D_{c,m} = \left(\frac{6\, q_c}{1000\, \pi\, N_c}\right)^{1/3}, D_{i,m} = \left(\frac{6\, q_{i,tot}}{\rho_{i,m}\, \pi\, N_{i,tot}}\right)^{1/3} \qquad (5a,b)$$

$$\rho_{i,m} = \frac{\int_0^\infty (m(D)^2/V(D))N(D)dD}{\int_0^\infty m(D)N(D)dD} \qquad (6)$$

$$r_{eff,c} = \frac{0.5\,(\mu_c+3)}{\lambda_c}, r_{eff,i} = \frac{3}{4}\frac{\int_0^\infty m(D)N(D)dD}{916.7\int_0^\infty A(D)N(D)dD} \qquad (7a,b)$$

where μ_c and λ_c are the shape and slope parameter of the cloud size distribution (MM15). $m(D)$, $A(D)$ and $N(D)$ are the mass-diameter, projected-area diameter and the PSD relationships for ice particles, respectively. $A(D)$ is given by Eq. (12) of Cholette et al. (2019), and $m(D)$ and $N(D)$ are described in Eq. (B6) and Eq. (2) in Cholette et al. (2023). $V(D) = \frac{\pi}{6}D^3$ is the volume of a sphere with the same particle diameter D.

To study the sensitivity in the choice of the ice nucleation parameterization, the fraction (in %) of the layer depth containing cloud liquid water. The coverage is computed as the vertical distance, which is the sum within the layer of vertical thicknesses between two levels where the cloud water content is > 0 g m^{-3}, divided by the total vertical distance of the layer.

https://doi.org/10.5194/egusphere-2026-4229
Preprint. Discussion started: 28 July 2026

The layers chosen are between 0–3 km, 3–4 km, 4–5 km and 5–6 km, which contain on average 20, 4, 4 and 3 vertical levels, respectively, in the 1-km simulations.

4. Results

4.1 Differences between BASE and AERO

At the initial time (i.e., 03 UTC 19 Jan 2026), the cloud system was already located in the Beaufort Sea (Fig. 2a). Overall cloud patterns and types are reasonably well represented by the simulations (Fig. 2b; AERO is identical to BASE, thus it is not shown in Fig. 2). After 21 h of simulation, at 00 UTC 20 Jan 2026, the system passed the Beaufort Sea and was located above and East of Inuvik (Fig. 2c). BASE (Fig. 2d) and AERO (Fig. 2e) show similar locations of the clouds and compare well with the location given by GOES-18 retrievals (Fig. 2c). AERO consistently shows higher outgoing infrared energy flux at model top compared with BASE (Fig. 2f), except at the initial time when there is no difference (not shown). Around Inuvik, values are higher by about 10–20 W m^{-2}, while in the southern part of the domain (including over the ocean and the west coast of Alaska and British Columbia) increases reached up to 45 W m^{-2}.

Cloud-top temperature is warmer in AERO than in BASE by about 5–6°C in the south and just southeast of Inuvik and 2–3°C warmer in the northern part (Fig. 3a–c). Southeast of Inuvik, cloud-top temperature in BASE decreases to -30°C and with cloud-top pressure between 450–550 hPa (not shown), whereas in AERO it is warmer and does not decrease below -27°C with higher cloud-top pressure (i.e., lower clouds) between 550–650 hPa. Precipitation accumulation is small, not exceeding 5 mm of liquid water equivalent in both BASE and AERO (Fig. 3d–f). The difference in precipitation accumulation between BASE and AERO (Fig. 3f) is small and spatially noisy (i.e., local increases and decreases), except in the southwest part of the domain over open water, where it is higher by about 0.6 mm, with total accumulation below 2 mm in AERO compared to BASE. Integrated CWC (Fig. 4a–b) is much smaller than integrated IWC (Fig. 5a–b), except along the northern coast of Alaska and over the Pacific Ocean located southwest. Integrated CWC is consistently larger in AERO than in BASE, whereas integrated IWC is generally lower (Fig. 4c, f).

In summary, after 21 h (on 00 UTC 20 Jan 2026) and also earlier (not shown), both BASE and AERO reproduce the observed cloud system location, indicating that the large-scale dynamics are well captured. AERO shows higher outgoing longwave radiation at the model top (by 10–45 $W \cdot m^{-2}$), consistent with warmer cloud-top temperatures (by 2–6°C) and lower cloud top heights near Inuvik. Despite these differences, total precipitation remains low and similar in both simulations. AERO also exhibits more liquid water and less ice, suggesting a shift in cloud phase that likely explains warmer clouds and enhanced infrared emission. Cloud phase is analysed in more detail in the next section.

https://doi.org/10.5194/egusphere-2026-4229
Preprint. Discussion started: 28 July 2026

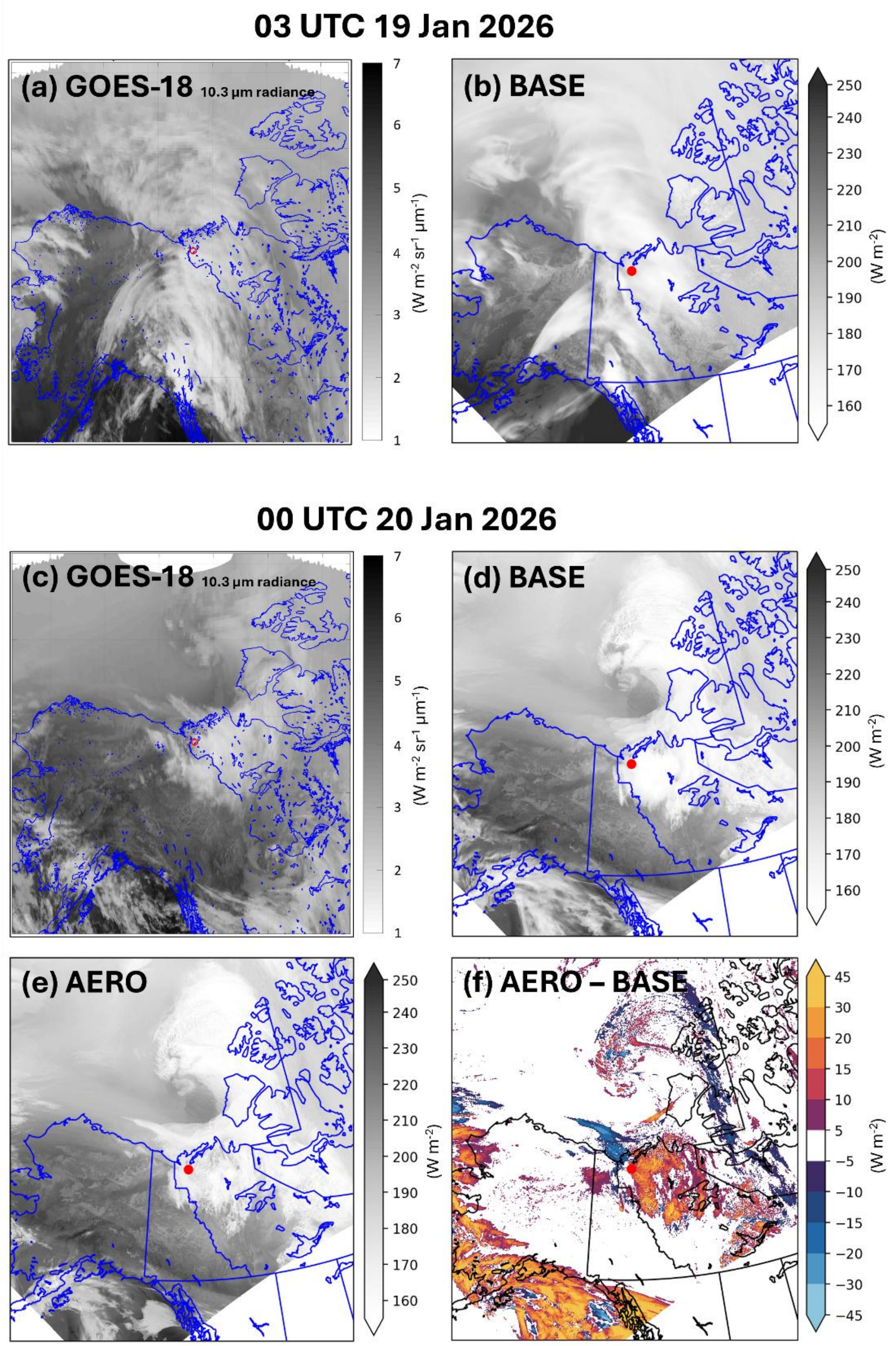

282

283 **Figure 2. (a and c) GOES-18 10.3 μm radiance (W m^{-2} sr^{-1} μm^{-1}), and (b and d) BASE, (e) AERO and (f) AERO – BASE outgoing**
284 **longwave radiation flux at the model top (W m^{-2}) on (a-b) 03 UTC 19 Jan 2026 and (c-f) 00 UTC 20 Jan 2026. The red dots show the**
285 **location of Inuvik.**

https://doi.org/10.5194/egusphere-2026-4229
Preprint. Discussion started: 28 July 2026

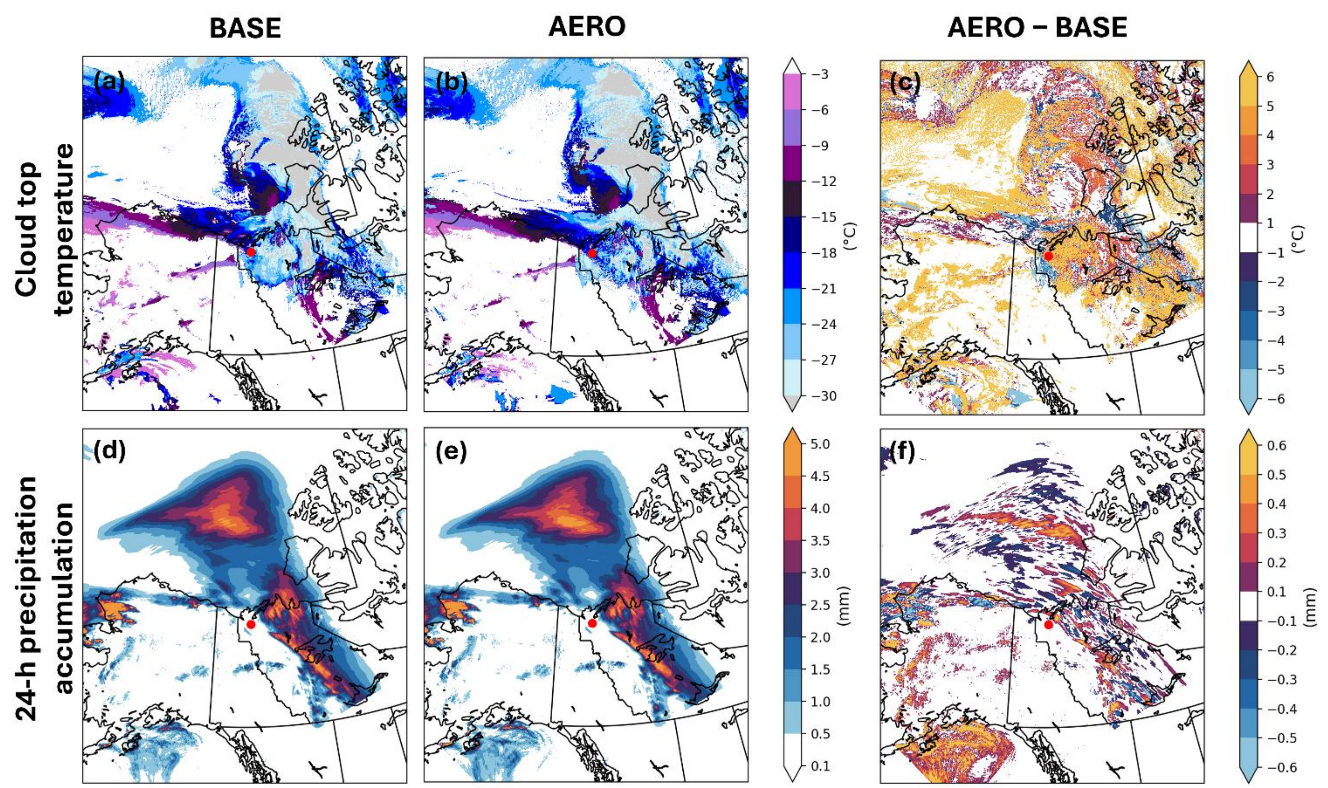

Figure 3. (a–c) Cloud top temperature (°C) and (d–f) 24-h accumulated total liquid-equivalent precipitation (mm) from (a and d) BASE, (b and e) AERO and (c, and f) AERO – BASE on 00 UTC 20 Jan 2026.

https://doi.org/10.5194/egusphere-2026-4229
Preprint. Discussion started: 28 July 2026

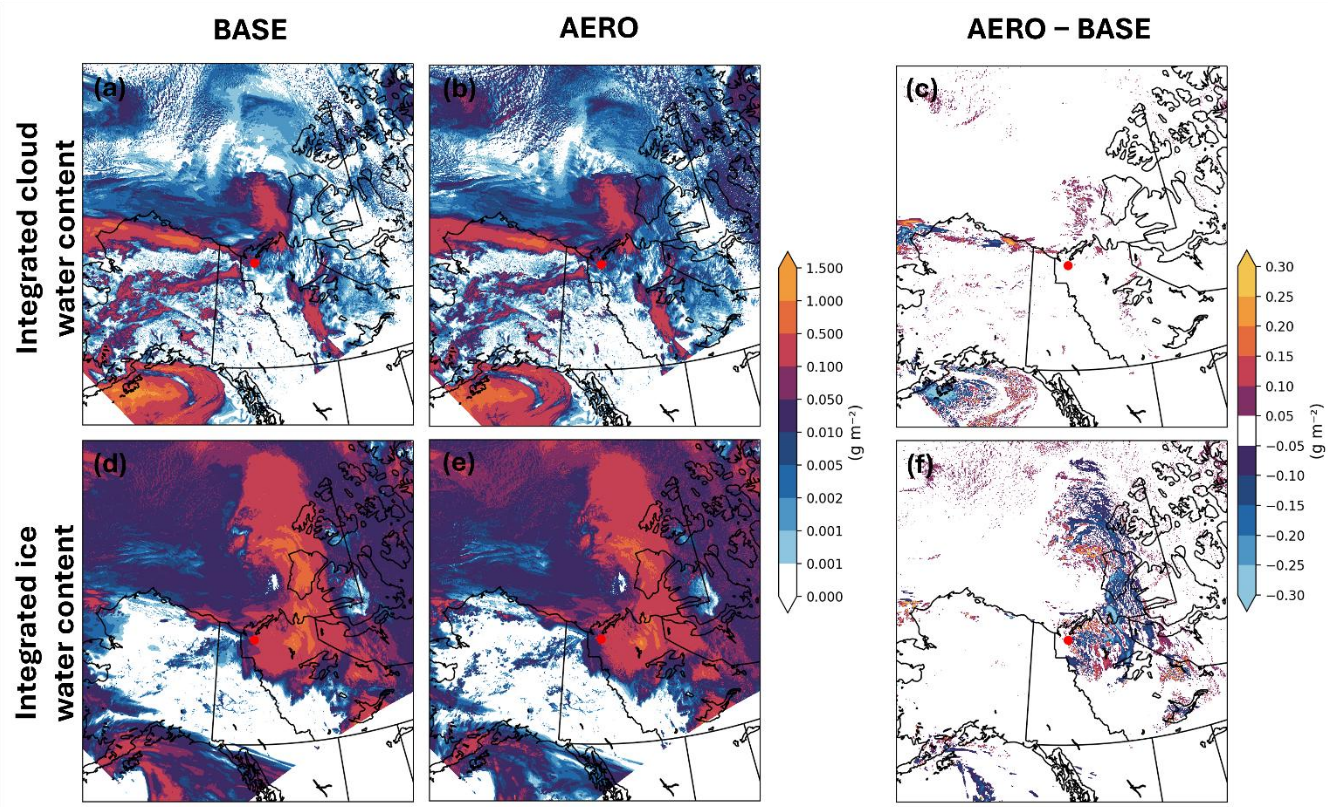

Figure 4. (a–c) Vertically integrated cloud water content (g m^{-2}) and (j–l) ice water content (g m^{-2}) from (a and d) BASE, (b and e) AERO and (c, and f) AERO – BASE on 00 UTC 20 Jan 2026.

4.2 Results at Inuvik

At Inuvik, atmospheric soundings every 6 h are shown in Fig. 5. BASE profiles (not shown) are very similar to those in AERO, except at 00 UTC on 20 Jan, where AERO is warmer by 0.5–1°C between 925–975 hPa, colder by less than 1°C at 900 hPa and warmer again by 1–1.5°C between 750–875 hPa. For all profiles, temperatures in the 1-km simulations are in better agreement than in CAPS at levels above 800 hPa, where CAPS is consistently warmer by about 5°C compared to the observations. This results from the higher number of vertical levels and improved vertical resolution in the 1-km simulations compared to CAPS. At 06 and 12 UTC on 19 Jan, at lower levels (below 800 hPa), although warmer between 800–900 hPa, simulations agree relatively well with the observed soundings, especially between 900–1000 hPa (Fig. 5a–b). Similar results are obtained at 18 UTC on 19 Jan and the simulations are warmer than the observations between 850–950 hPa. The observed temperature inversions are well captured by AERO throughout the day. In all soundings, the simulated surface temperature is lower than observed in both CAPS and the 1-km simulations. This bias is reduced in the 1-km simulations, especially for 12 and 18 UTC 19 Jan, but also at 00 UTC 20 Jan. The saturated layer at 875 hPa observed at 18 UTC on 19 January is missed by all simulations (Fig. 5c) but the one at 00 UTC 20 Jan is well captured by BASE (not shown) and AERO (Fig. 5d).

https://doi.org/10.5194/egusphere-2026-4229
Preprint. Discussion started: 28 July 2026

The temporal evolution of near-surface air temperature shows that all simulations are generally colder by 5°C compared to observations and the 1-km simulations are warmer than CAPS by about 0.5–4°C (Fig. 6a). The cold bias obtained in operational CAPS is similar in magnitude to Casati et al. (2023), however it is of the opposite sign: a warm bias for the cold season was shown in Casati et al. (2023). That warm bias was primarily explained by an overprediction of low-level Arctic clouds, which increased downward longwave radiation and warmed the near-surface atmosphere, an effect that was partly masked in uncoupled simulations by errors in the initialization of sea-ice temperature (pers. comm. with Dr. J.-P. Paquin). This issue is expected to be corrected in the next operational version of CAPS. Regardless of the sign of the bias in CAPS, since it is used to provide the initial and lateral boundary conditions to the 1-km simulations, it is expected that the bias is partially transferred to the nested simulations. However, local processes resolved at higher resolution, as well as changes to the model physics (e.g., the use of P3 with prognostic aerosols), may modulate its magnitude.

Relative humidity with respect to water is lower in the simulations than in the observations by 2–10% and is similar between the 1-km simulations and CAPS, except for some hours for which it is slightly higher in CAPS (Fig. 6b). Near-surface pressure increases slightly over time at Inuvik, which is well captured by the simulations, although CAPS shows lower pressures and the 1-km simulations are higher than the observations (Fig. 6c).

Precipitation rate is very low in the simulations and zero in the observations (Fig. 6d). It is typical for WXT to report zero when trace precipitation occurs as the instrument is not sensitive enough to detect. The MRR-PRO reflectivity (Fig. 7a) shows clouds above Inuvik at: 0300, 0430, 0800, 1030 and 1830–2200 UTC 19 Jan, with very light precipitation reaching the surface, especially around 08 UTC on 19 Jan. The simulations show similar behaviour and AERO shows higher reflectivity than BASE throughout the event between 1830 and 22 UTC on 19 Jan (Fig. 7c–d). Reflectivity is overestimated in all simulations after 23 UTC 19 Jan but underestimated in magnitude compared to the MRR before that time.

Vertical profiles of the two new prognostic variables, $N_{a,w}$ and $N_{a,i}$, at the beginning of the AERO simulation and after 21 h (at 00 UTC on 20 Jan) show the history of altitudes at which clouds form. $N_{a,w}$ is between 2×10^8 and 5×10^8 m^{-3} and always higher than $N_{a,i}$, which ranges between 5×10^4 and 5×10^5 m^{-3} (Fig. 8). This is consistent with climatological values for that time of the year and region (Colarco et al., 2010). At the initial time, both $N_{a,w}$ and $N_{a,i}$ increase with decreasing height, except near the lowest levels, and initial maxima occur at around 1.5 km and 3 km for $N_{a,w}$ and $N_{a,i}$, respectively. After 21 h, both profiles are reduced at altitudes where clouds formed or where collection and freezing processes occurred. The increases in both $N_{a,w}$ and $N_{a,i}$ at lower levels (near 2 km for $N_{a,w}$ and 3 km for $N_{a,i}$) after 21 h compared with the initial state are associated with regions where evaporation and sublimation occurred.

In summary, at Inuvik, the simulated vertical temperature structure agrees reasonably well with the observations, especially for the 1-km simulations which reduce the warm bias aloft (< 800 hPa) and better capture the temperature inversion and saturated layers compared to CAPS. However, all simulations exhibit a cold bias at the surface relative to the observations, although this bias is reduced in the 1-km simulations compared to CAPS. Cloud events detected by the MRR over Inuvik are broadly reproduced by the simulations, but the simulated reflectivity is often weaker than observed. The vertical analysis of

https://doi.org/10.5194/egusphere-2026-4229
Preprint. Discussion started: 28 July 2026

aerosol number concentrations shows realistic magnitudes compared to the climatology and vertical distributions as well as multiple cloud layers formed over Inuvik.

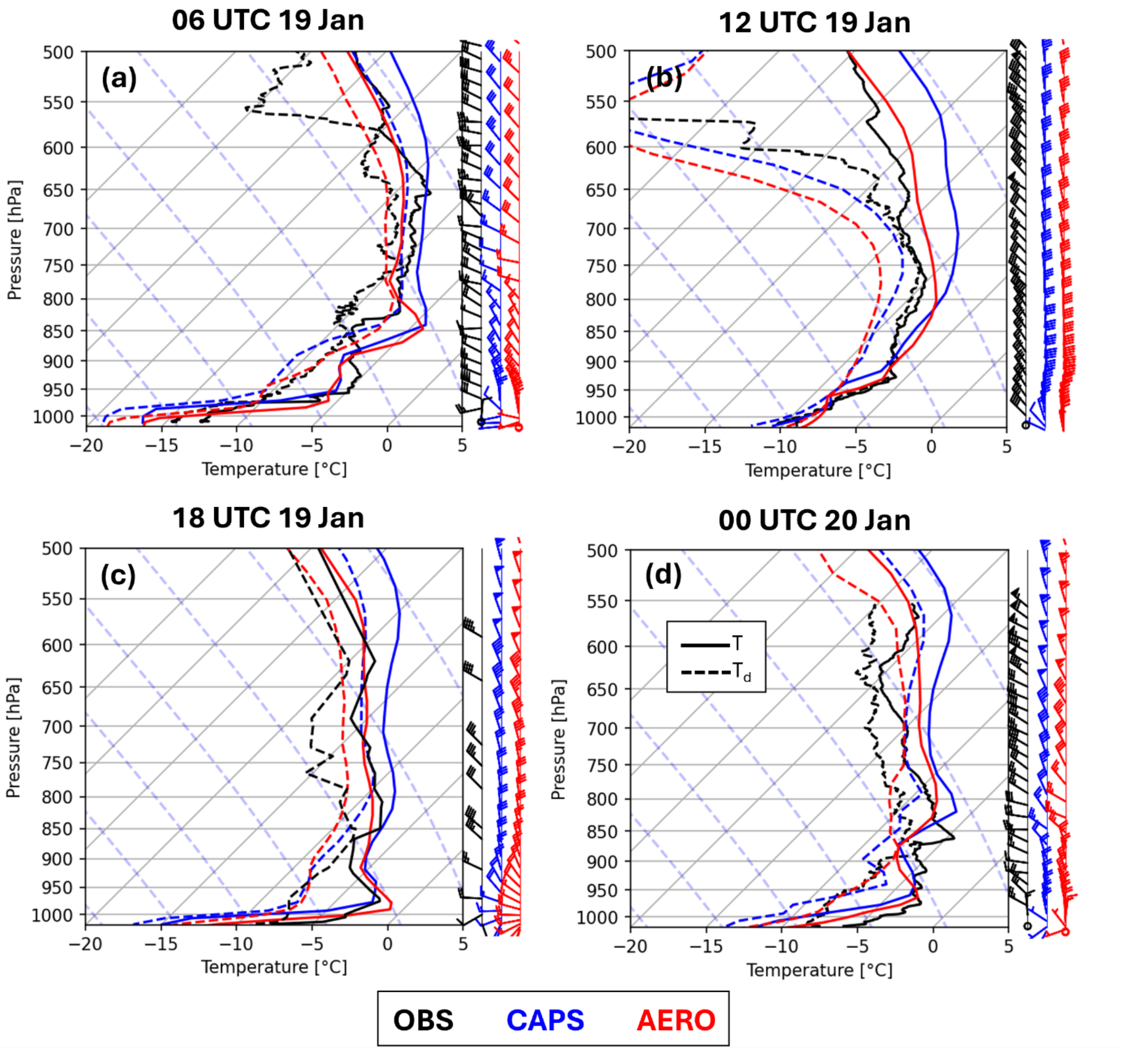

Figure 5. (a) 06 UTC 19 Jan, (b) 12 UTC 19 Jan, (c) 18 UTC 19 Jan and (d) 00 UTC 20 Jan vertical profiles at Inuvik of temperature (solid; °C), dew point temperature (dashed; °C), and wind speeds and directions (barbs with flags, pennants, and half-pennants denoting 50, 10, and 5 knots, respectively) from observed soundings (black), CAPS (blue) and AERO (red). All observed soundings are from the ECCC high-resolution archive.

https://doi.org/10.5194/egusphere-2026-4229
Preprint. Discussion started: 28 July 2026

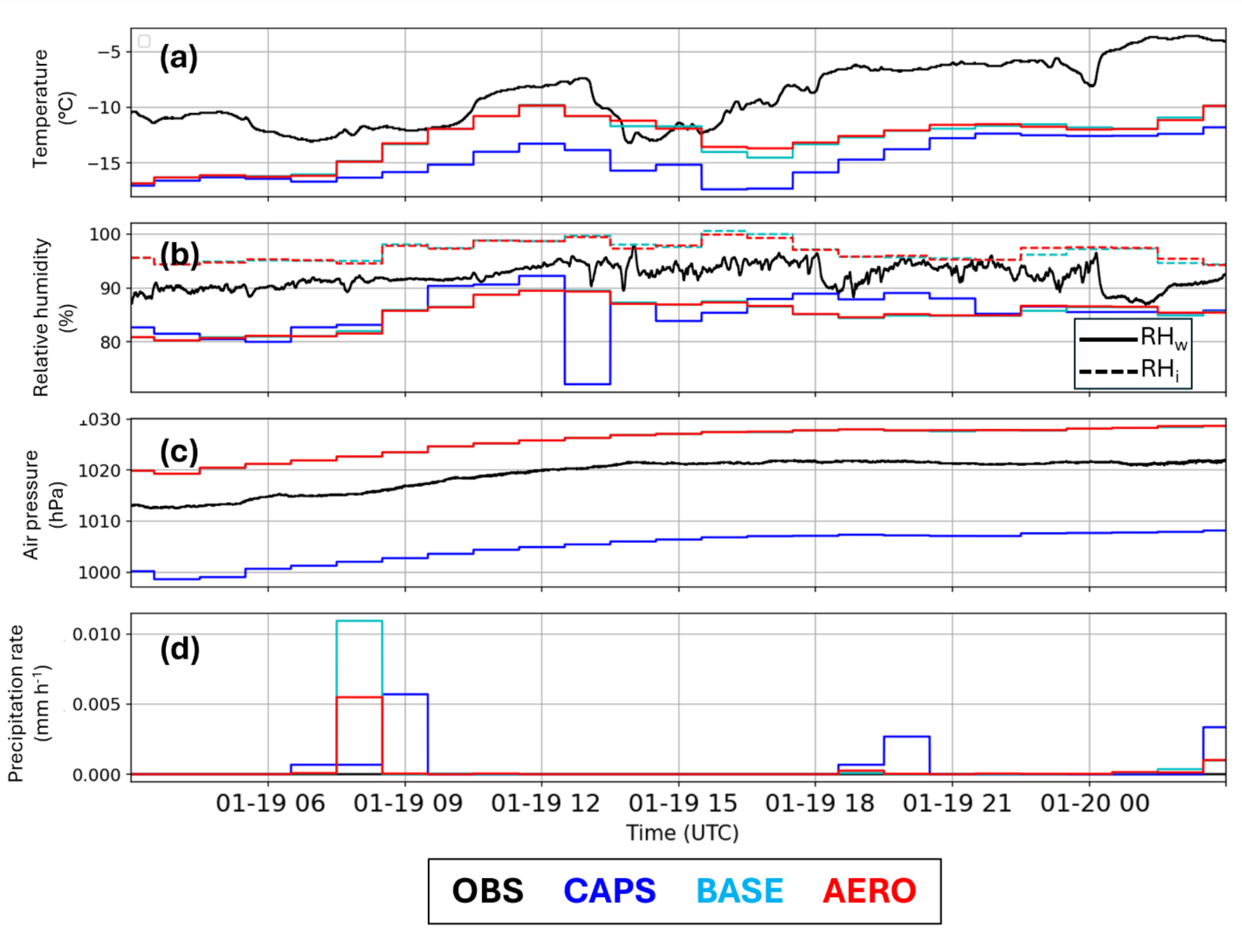

Figure 6. Time series at Inuvik of (a) near surface temperature (°C), (b) relative humidity (%), (c) near-surface pressure (hPa) and (d) precipitation rate (mm h^{-1}) for WXT536 observations (black), CAPS (dark blue), BASE (light blue) and AERO (red). In (b), solid lines are relative humidity with respect to water (RH$_w$), and the dashed lines are relative humidity with respect to ice (RH$_i$) of BASE and AERO only.

https://doi.org/10.5194/egusphere-2026-4229
Preprint. Discussion started: 28 July 2026

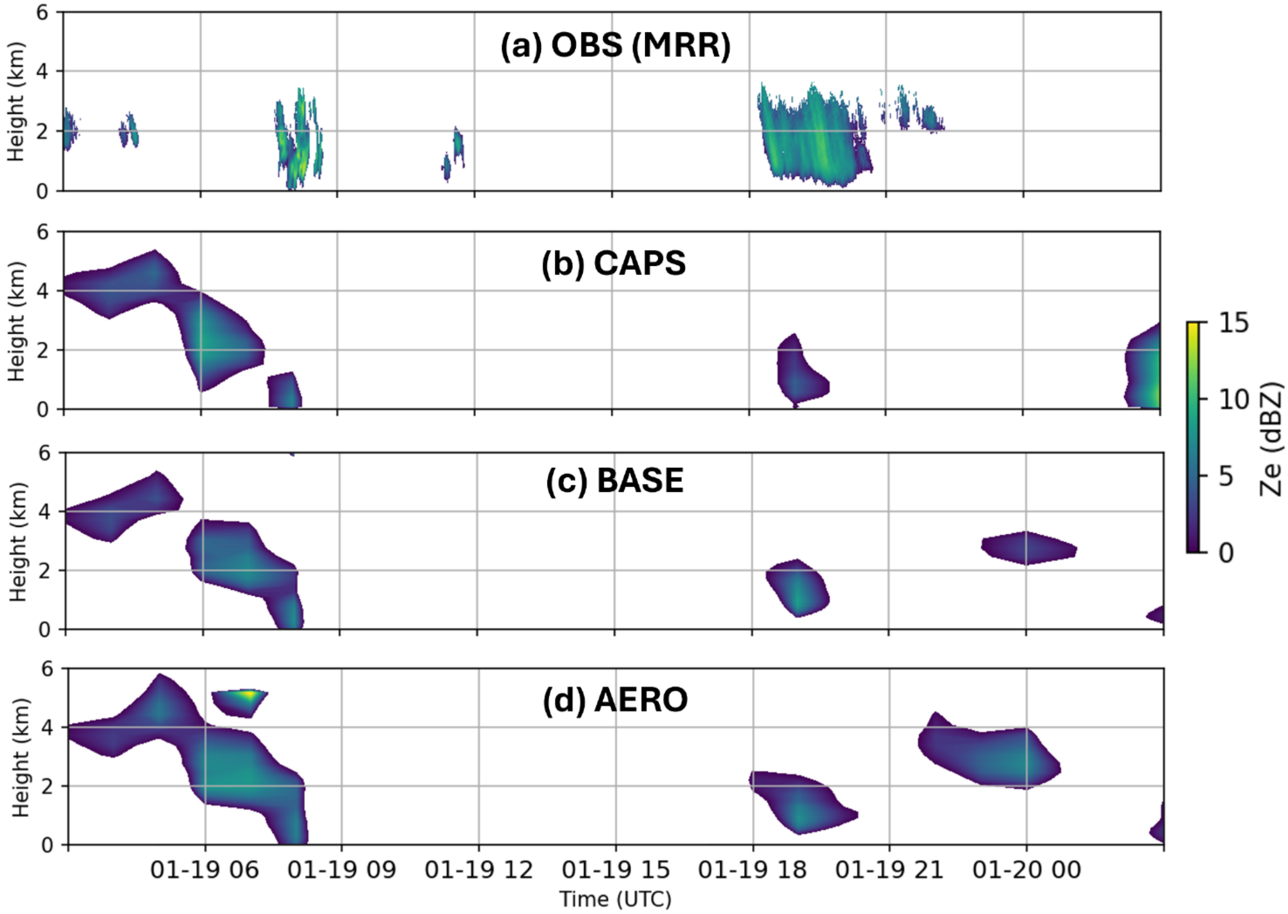

Figure 7. Time series at Inuvik of reflectivity (dBZ) from (a) MRR, (b) CAPS, (c) BASE and (d) AERO.

https://doi.org/10.5194/egusphere-2026-4229
Preprint. Discussion started: 28 July 2026

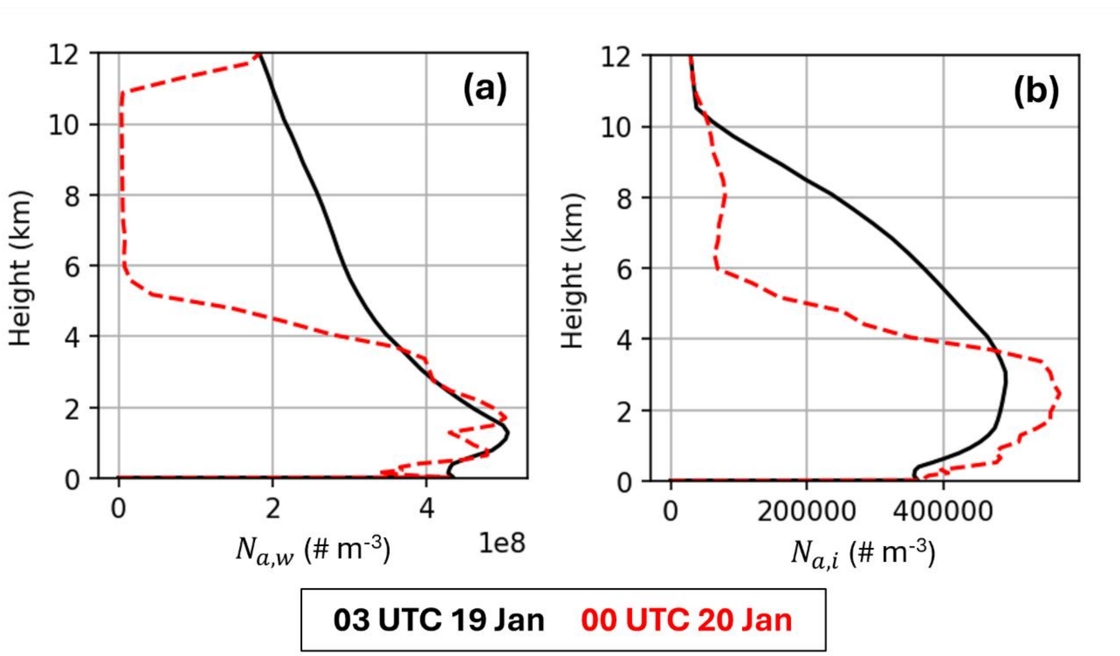

Figure 8. Initial (black; at 03 UTC 19 Jan) and after 21 h forecast (dashed red; at 00 UTC 20 Jan) vertical profiles at Inuvik of (a) $N_{a,w}$ (m^{-3}) and (b) $N_{a,i}$ (m^{-3}) from AERO.

4.3 Comparison along the EarthCARE path

Apart from the reflectivity comparison, which shows the overall good performance of CAPS, the analysis along the EarthCARE track for frame 09352C, which started at 23:50:49 UTC on 19 January 2026, focuses on the differences between BASE and AERO in the 1-km configuration.

Based on the observed reflectivity on 00 UTC on 20 Jan (Fig. 9a), there are two different types of cloud regimes along the track. To the south (between 67.5° and 70.5° latitude) near Inuvik (68.4° latitude), the cloud field, hereafter referred to as type A, is associated with the post-frontal system at that time. In type A, cloud tops reach 8 to 10 km and the clouds are generally composed of thin ice containing embedded supercooled liquid layers (Figs. 10a and 12a, respectively). To the north (between 72° and 75° latitude), the cloud field, hereafter referred to as type B, is a broad Arctic stratiform mixed-phase cloud system with embedded generating cells (Figs. 10a and 12a).

Model-equivalent reflectivity, computed following Cholette et al. (2023), is similar to the observed reflectivity in all simulations, with the 1-km simulations reproducing the observed features better than CAPS, particularly for the generating cells in type B (Fig. 9b–d). The 1-km simulations also show two cloud layers between type A and type B, near 70° to 72° latitude. The first layer consists of low-level clouds located between 0 and 1 km height which are simulated in the 1-km runs but not in CAPS, and the second layer, simulated in all runs, is at approximately 3 to 5 km height and is an extension of the

https://doi.org/10.5194/egusphere-2026-4229
Preprint. Discussion started: 28 July 2026

thin ice-cloud layer associated with the post frontal system of type A. At Inuvik and at that time, even though the MRR-PRO dBZ sensitivity goes down to -8 dBZ, it failed at detecting the cloud signal at 6-km height (Fig. 7a) that is detected in EarthCARE retrievals with values around -4 dBZ (Fig. 9a) probably due to instrument sensitivity limits, attenuation and signal-to-noise ratio.

The observed cirrus at an altitude of 10-km in type A does not appear in the simulated reflectivity fields because the simulated reflectivity remains below the threshold used in the figure: it is, however, clearly seen in the IWC field (Fig. 10a–c). Cloud tops in type A reach up to 10 km in both the EarthCARE retrievals and the simulations with a maximum reflectivity near 10 dBZ at around 69° latitude, which is captured well by all simulations, although the exact location varies among CAPS, BASE and AERO. Type B clouds are reproduced well by all simulations, especially by the 1-km simulations which show improved vertical structure of the generating cells compared to CAPS. This is because of the finer horizontal and vertical grid spacings in the 1-km simulations. The type A cloud system has lower reflectivity than the type B system, a feature captured well by all simulations.

Notable differences between BASE and AERO occur in both types A and B. First, the IWC in AERO is 0.5 to 1 g m^{-3} lower than in BASE (Fig. 10d) throughout most regions of type A, including the cirrus region (near 8–10 km). Clouds in type B, composed predominantly of ice, are well reproduced by the simulations and the IWC exhibits significant differences between AERO and BASE within the generating cells (Fig. 10d). Near the cloud base in type B, higher IWC is obtained in AERO compared to BASE associated with the presence of ice in AERO, which is absent in BASE. The ice effective radius is higher in simulations compared to the retrievals (Fig. 11). It is 10–30 µm higher in AERO compared to BASE, particularly at altitudes above 5 km in type A and near cloud top in type B (Fig. 11). All the simulations clearly struggle to reproduce the embedded supercooled liquid layers in type A (Fig. 12a–c) and only AERO simulates some of the layers with locations and heights that differ from the retrievals. In type B, the supercooled liquid layer at cloud top is not well represented in CAPS (not shown), but it is better reproduced in the 1-km simulations, particularly in AERO relatively to BASE (Fig. 12b–c). The simulated cloud droplet effective radius is similar or slightly higher by 10 µm in both simulations compared to the EarthCARE retrievals (Fig. 13). The cloud droplet effective radius is larger in AERO than in BASE where liquid clouds are present in both simulations.

The differences between the simulated cloud properties are analysed next, starting by showing the two new prognostic variables $N_{a,w}$ and $N_{a,i}$ in AERO at two different times are shown in Fig. 14 along the EarthCARE track. At initial time, aerosol number vertical profiles are similar to the vertical profiles shown in Fig. 8, with values increasing toward lower altitudes. At a forecast time of 21 h, both $N_{a,w}$ and $N_{a,i}$ decrease in regions where clouds formed earlier in the simulation or where aerosols were collected by the solid or liquid hydrometeors. During the simulation, $N_{a,w}$ and $N_{a,i}$ increase mainly in regions of evaporation and sublimation, respectively. The large decrease in $N_{a,w}$ and $N_{a,i}$ obtained between 5–9 km height at 67–71° latitude results from cloud and ice nucleation.

AERO is approximately 1°C colder than BASE at around 5 km height in the type A cloud system (Fig. 15a–b), which also corresponds to a region of higher relative humidity with respect to water (not shown) and ice (Fig. 15c–d). Above (below) this

https://doi.org/10.5194/egusphere-2026-4229
Preprint. Discussion started: 28 July 2026

region, AERO is similar (warmer) than BASE in type A. AERO is also slightly colder immediately above cloud top, but remains similar to BASE below the supercooled liquid layer in type B.

The ice number concentration is always lower in AERO compared to BASE and, in regions where the IWC is lower, this results in larger mass-weighted mean ice particle diameters (Fig. 16a–d), which explains that AERO exhibits higher reflectivity than BASE. Where the ice effective radius is smaller, typically near cloud tops, the mass-weighted mean density of ice in AERO is lower by 200–300 kg m^{-3} (Fig. 16e–f). In the type B clouds, the rime mass fraction is higher in AERO (Fig. 16g–h), which is a consequence of enhanced riming within the liquid cloud layer near the cloud top.

In summary, over the satellite track, AERO consistently produces larger ice particles than BASE because of lower ice number concentrations, leading to higher reflectivity in both the type A and type B cloud regimes. This result agrees with respect to the MRR data of Fig. 7. In type A, AERO simulates some supercooled liquid layers that are largely absent in BASE, while exhibiting lower IWC overall (by 0.5–1 g m^{-3}). This combination of fewer but larger ice particles results in larger ice effective radii (by 10–30 µm), especially above 5 km, which impacts radiative transfer in the simulation. In type B, AERO better reproduces the supercooled liquid layer at cloud top from the satellite retrieval. Additionally, AERO tends to be slightly colder within mixed-phase cloud regions (e.g., around 5 km in type A and near cloud top in type B), which contributes to higher relative humidity and enhanced microphysical processes, such as riming as reflected by a higher rime mass fraction. Overall, the differences between AERO and BASE are mainly driven by changes in ice microphysics, resulting in fewer, larger, and more heavily rimed ice particles in AERO.

https://doi.org/10.5194/egusphere-2026-4229
Preprint. Discussion started: 28 July 2026

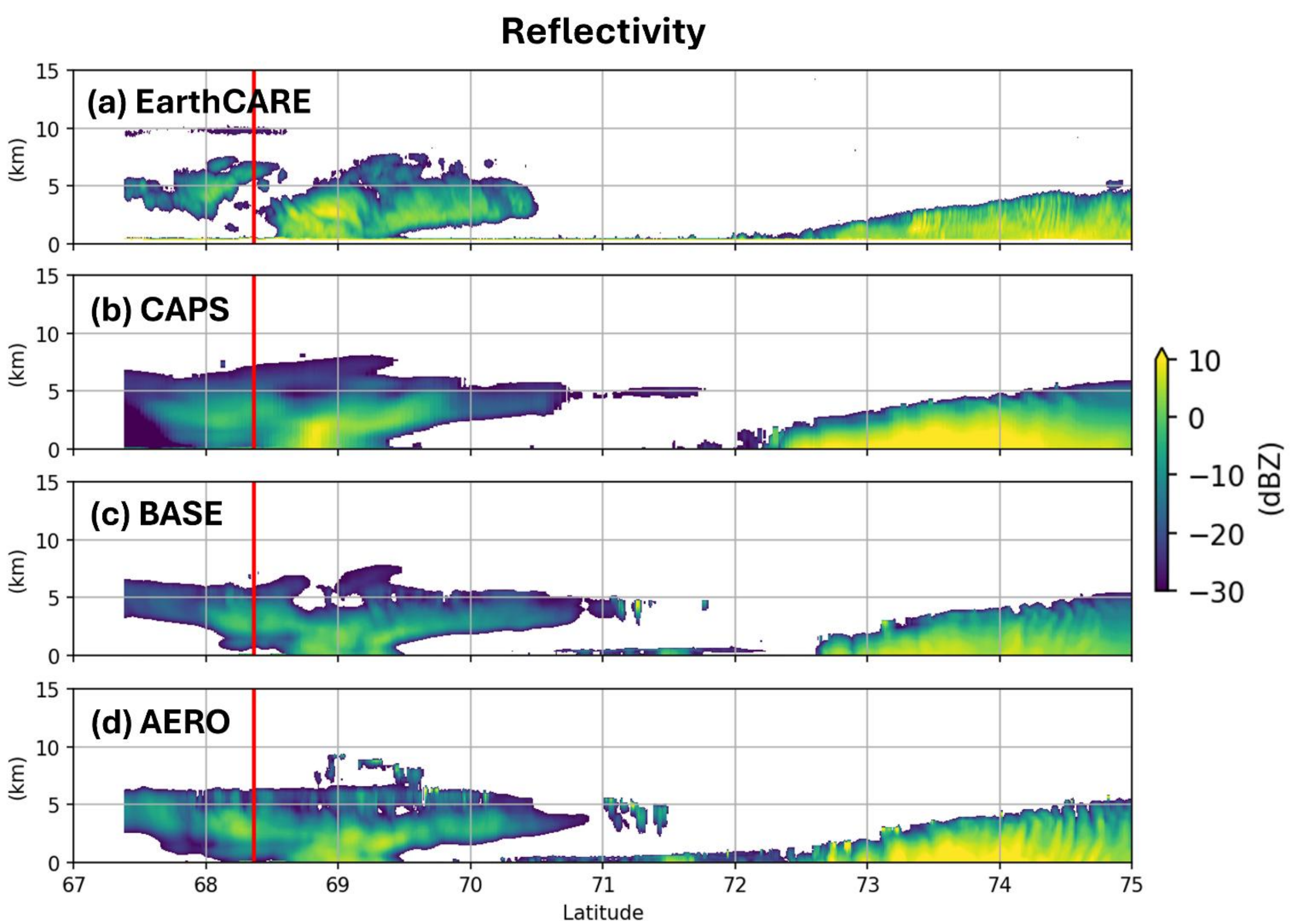

Figure 9. Reflectivity (dBZ) from (a) EarthCARE retrievals (ACM-CAP, Baseline BC), (b) CAPS, (c) BASE and (d) AERO along the EarthCARE pass on 00 UTC 20 Jan. The vertical red lines show the latitude of Inuvik.

https://doi.org/10.5194/egusphere-2026-4229
Preprint. Discussion started: 28 July 2026

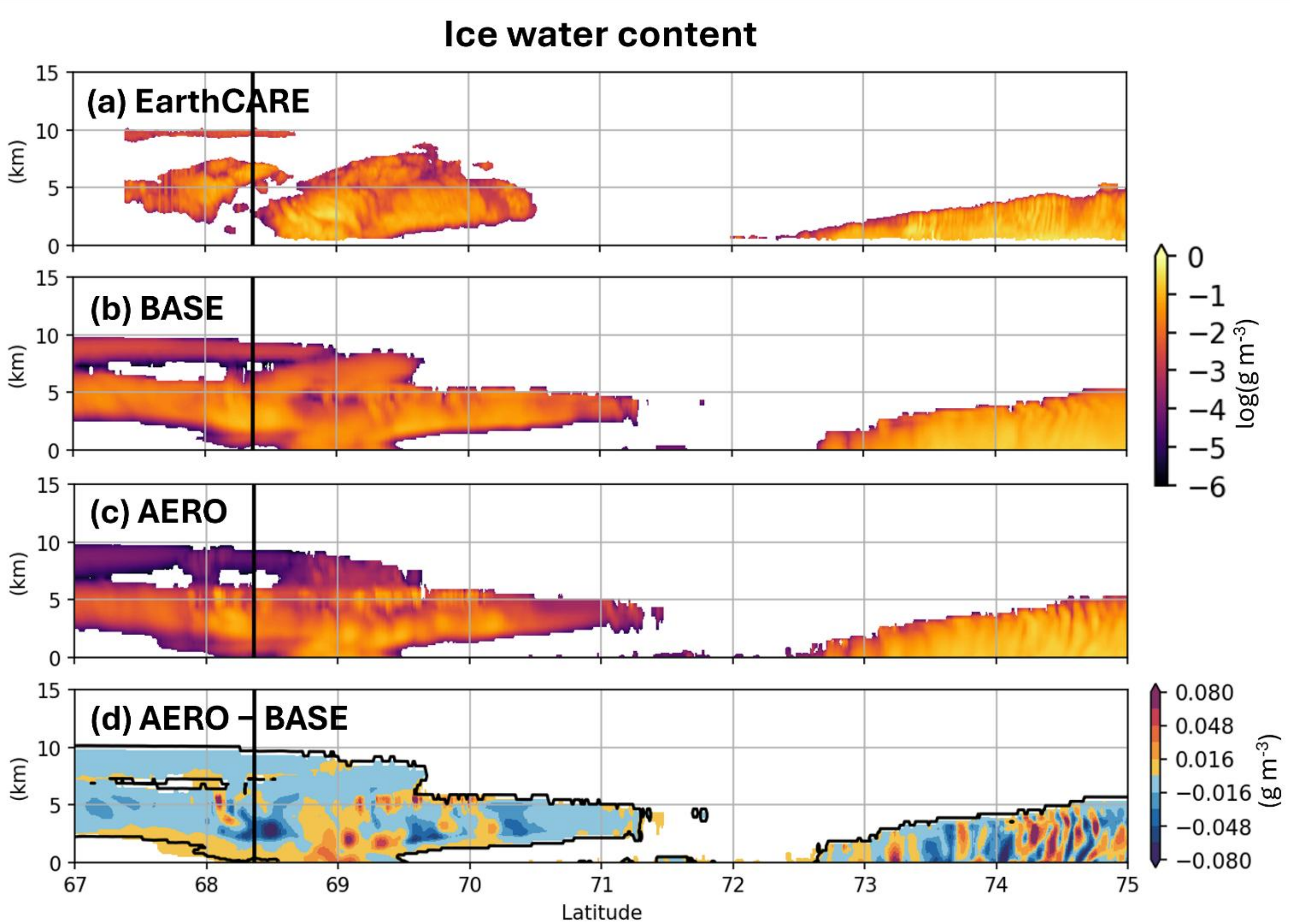

Figure 10. Ice water content (IWC; g m^{-3}) from (a) EarthCARE retrievals (ACM-CAP, Baseline BC), (b) BASE, (c), AERO and (d) AERO – BASE along the EarthCARE pass on 00 UTC 20 Jan. Note that EarthCARE data at latitudes lower than 67.5° are not available. The black line in (d) is where IWC is > 0 in BASE. The vertical black lines show the latitude of Inuvik.

https://doi.org/10.5194/egusphere-2026-4229
Preprint. Discussion started: 28 July 2026

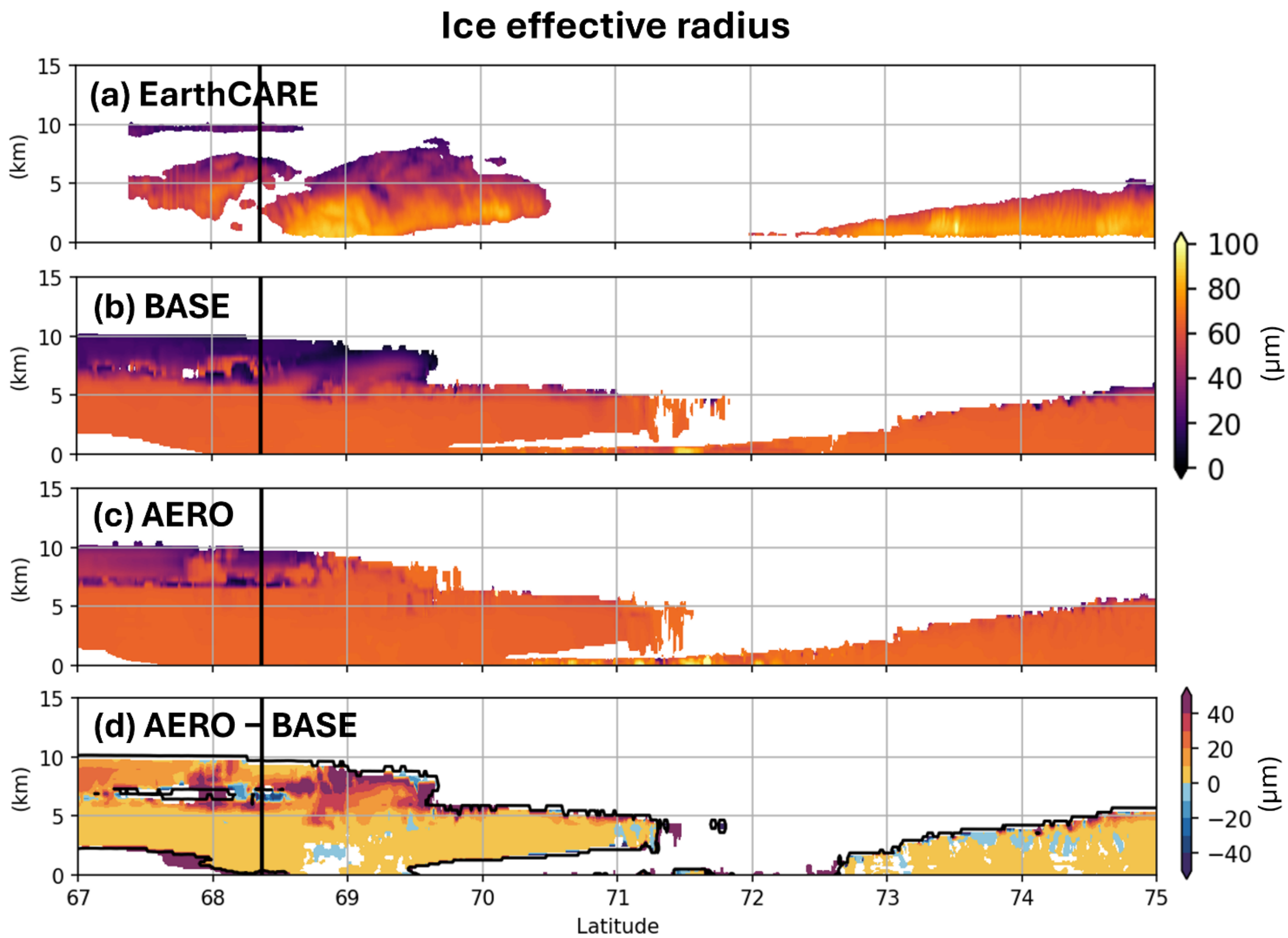

Figure 11. Ice effective radius ($r_{eff,i}$; μm) from (a) EarthCARE retrievals (ACM-CAP, Baseline BC), (b) BASE, (c), AERO and (d) AERO – BASE along the EarthCARE pass on 00 UTC 20 Jan. Note that EarthCARE data at latitudes lower than 67.5° are not available. The black line in (d) is where $r_{eff,i}$ is > 0 in BASE. The vertical black lines show the latitude of Inuvik.

https://doi.org/10.5194/egusphere-2026-4229
Preprint. Discussion started: 28 July 2026

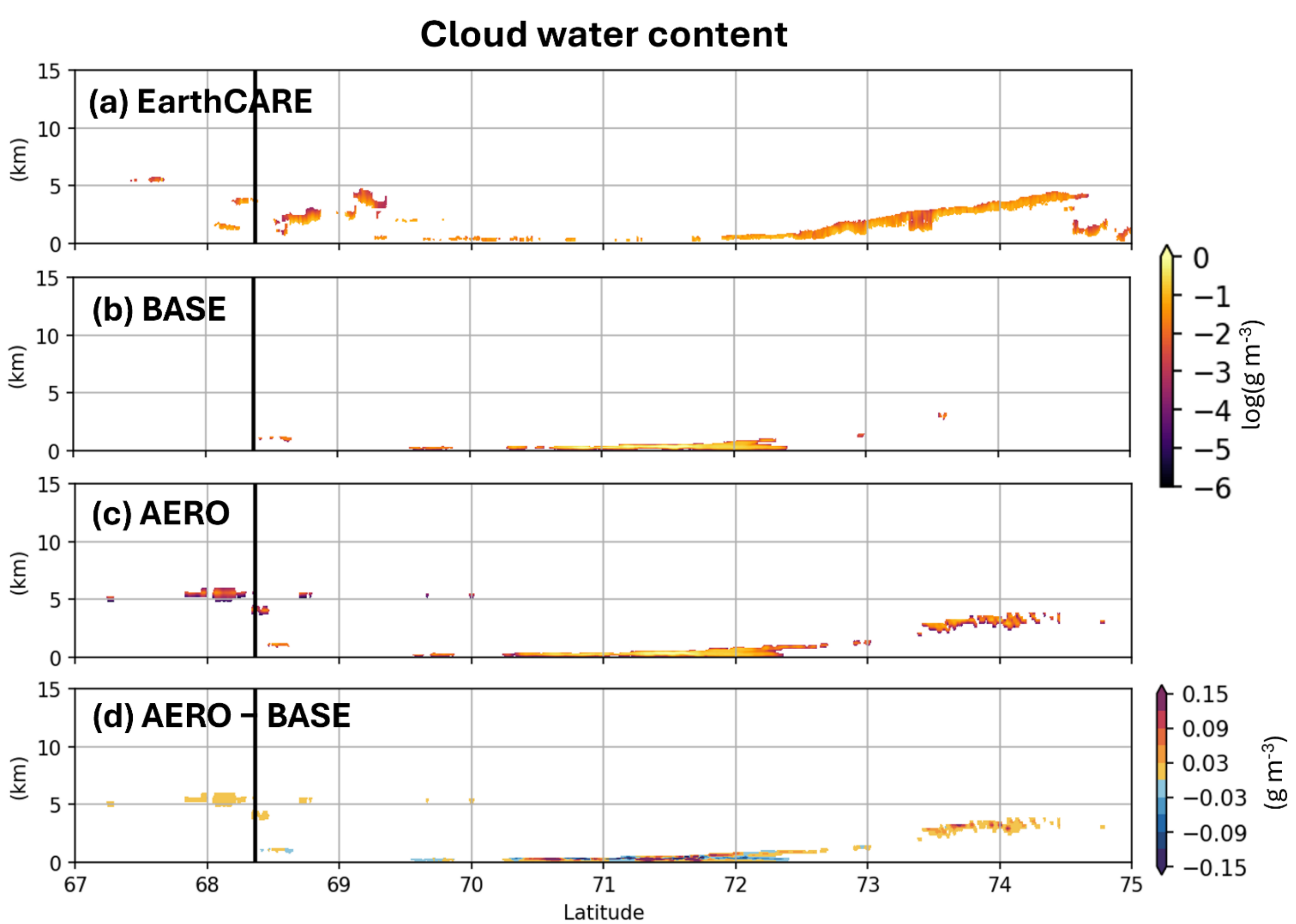

Figure 12. Liquid water content (CWC; g m^{-3}) from (a) EarthCARE retrievals (ACM-CAP, Baseline BC), (b) BASE, (c), AERO and (d) AERO – BASE along the EarthCARE pass on 00 UTC 20 Jan. Note that EarthCARE data at latitudes lower than 67.5° are not available. The vertical black lines show the latitude of Inuvik.

https://doi.org/10.5194/egusphere-2026-4229
Preprint. Discussion started: 28 July 2026

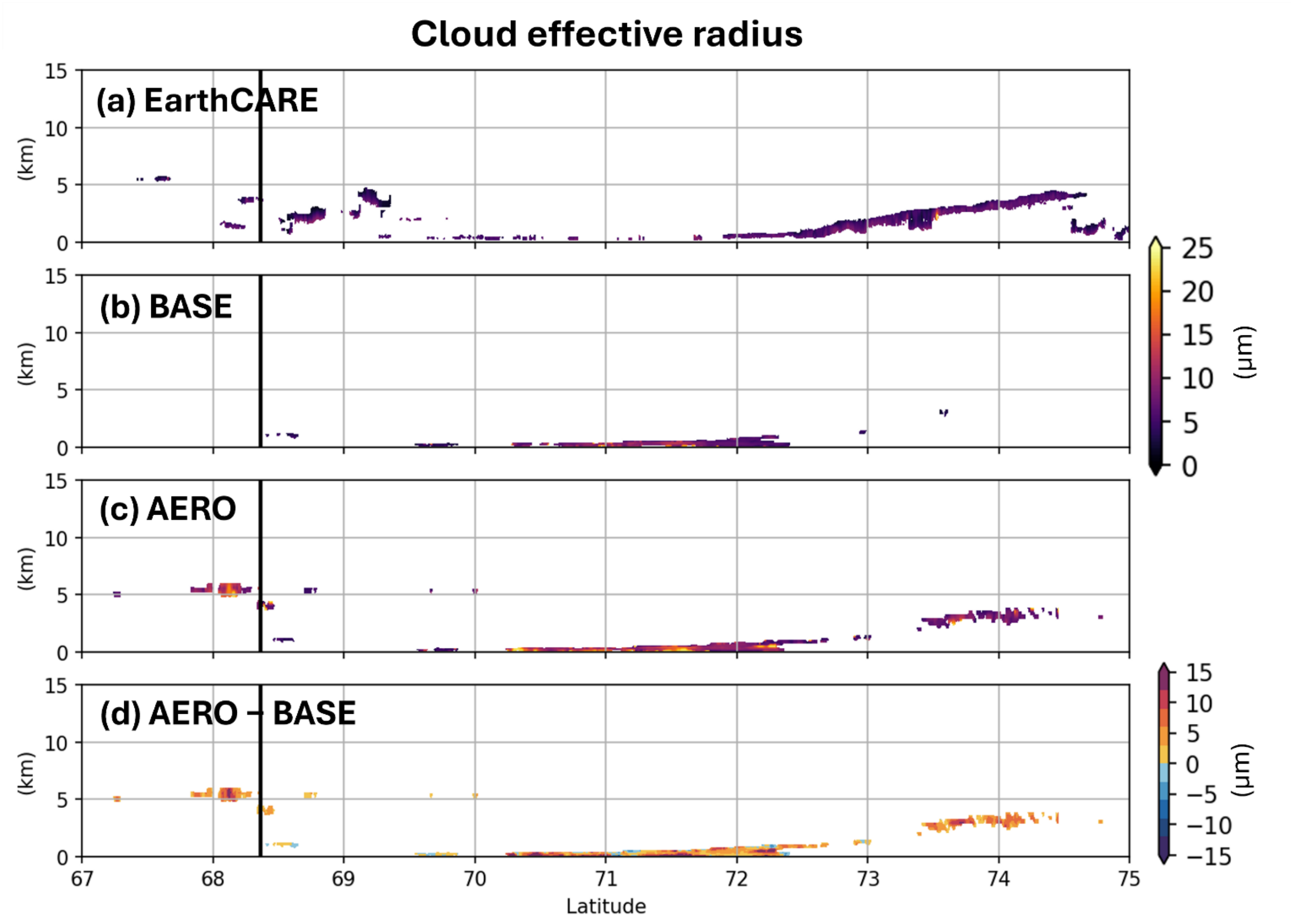

446

447 **Figure 13. Cloud droplet effective radius ($r_{eff,c}$; μm) from (a) EarthCARE retrievals (ACM-CAP, Baseline BC), (b) BASE, (c),**
448 **AERO and (d) AERO – BASE along the EarthCARE pass on 00 UTC 20 Jan. Note that EarthCARE data at latitudes lower than**
449 **67.5° are not available. The vertical black lines show the latitude of Inuvik.**

450

https://doi.org/10.5194/egusphere-2026-4229
Preprint. Discussion started: 28 July 2026

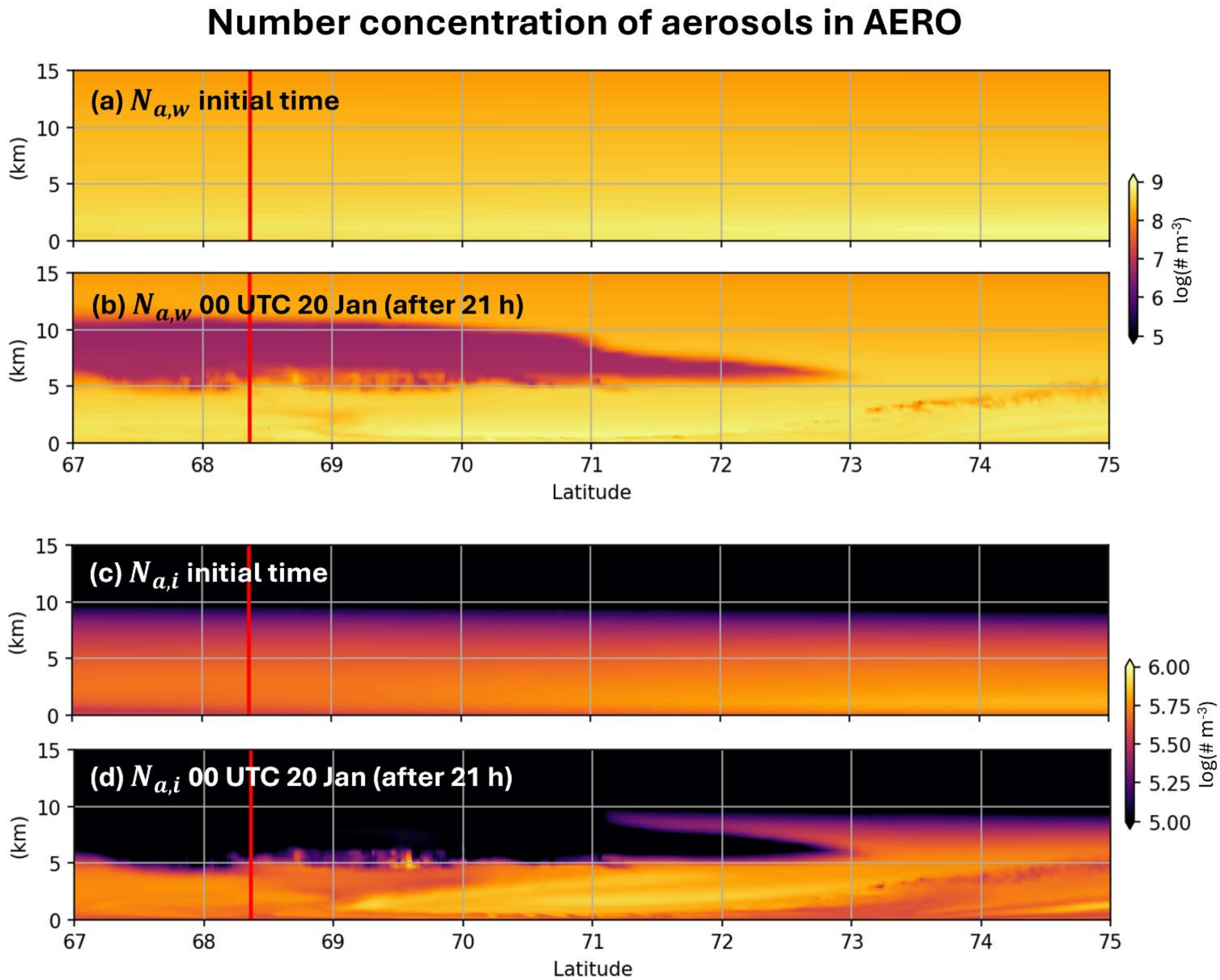

Figure 14. (a and b) Number of water-friendly aerosols ($N_{a,w}$; m^{-3}) and (c and d) Number of ice-friendly aerosols ($N_{a,i}$; m^{-3}) from AERO at (a and c) initial time (03 UTC 19 Jan) and (b and d) at 21 h forecast time (00 UTC 20 Jan). The vertical red lines show the latitude of Inuvik.

https://doi.org/10.5194/egusphere-2026-4229
Preprint. Discussion started: 28 July 2026

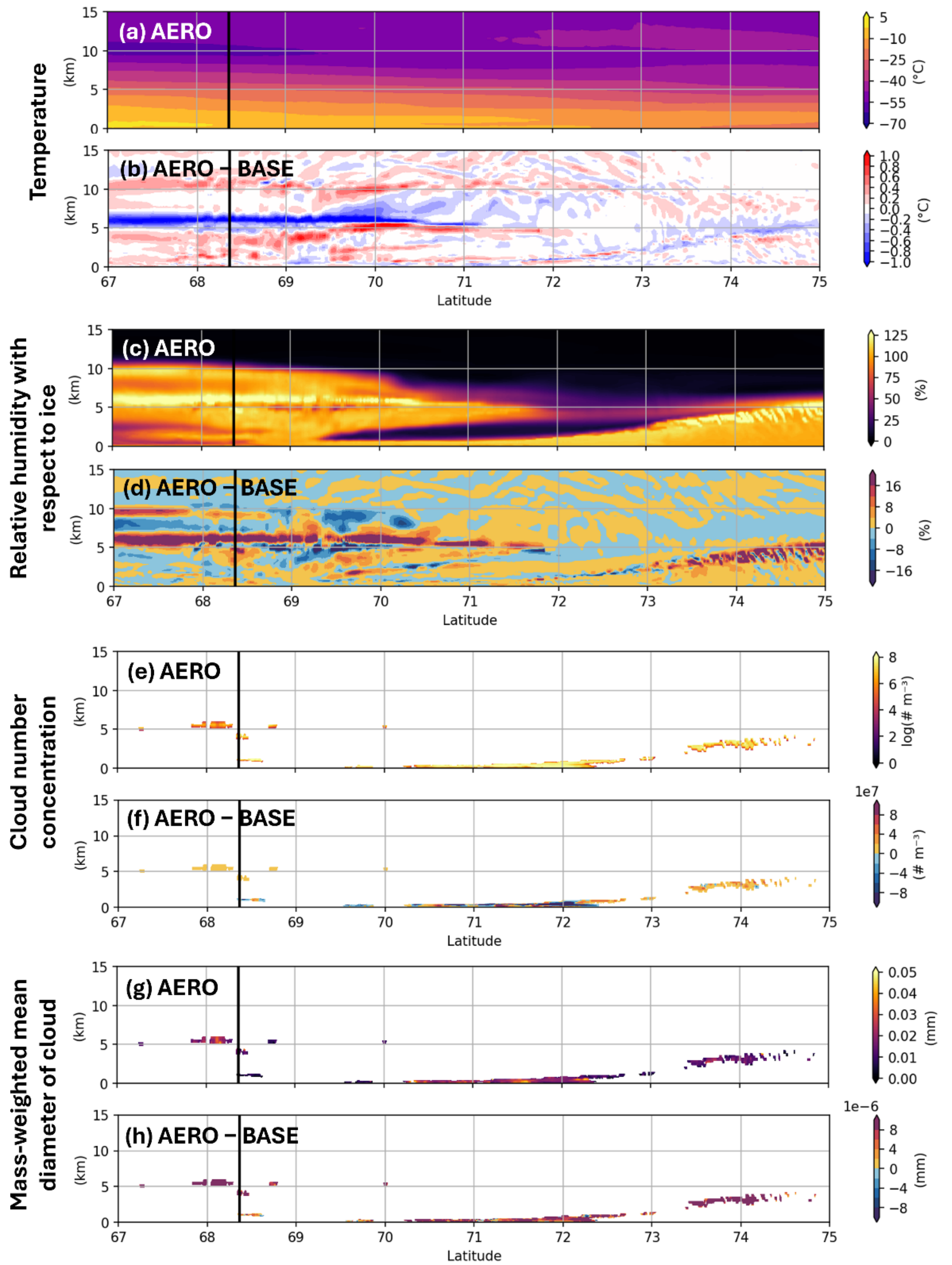

Figure 15. (a, c, e and g) AERO and (b, d, f and h) AERO – BASE along the EarthCARE pass on 00 UTC 20 Jan of (a–b) temperature (*T*; °C), (c–d) relative humidity with respect to ice (RH_i; %), (e–f) cloud number concentration (N_c; # m^{-3}) and (g–h) mass-weighted mean diameter of cloud ($D_{c,m}$; mm). The vertical black lines show the latitude of Inuvik.

https://doi.org/10.5194/egusphere-2026-4229
Preprint. Discussion started: 28 July 2026

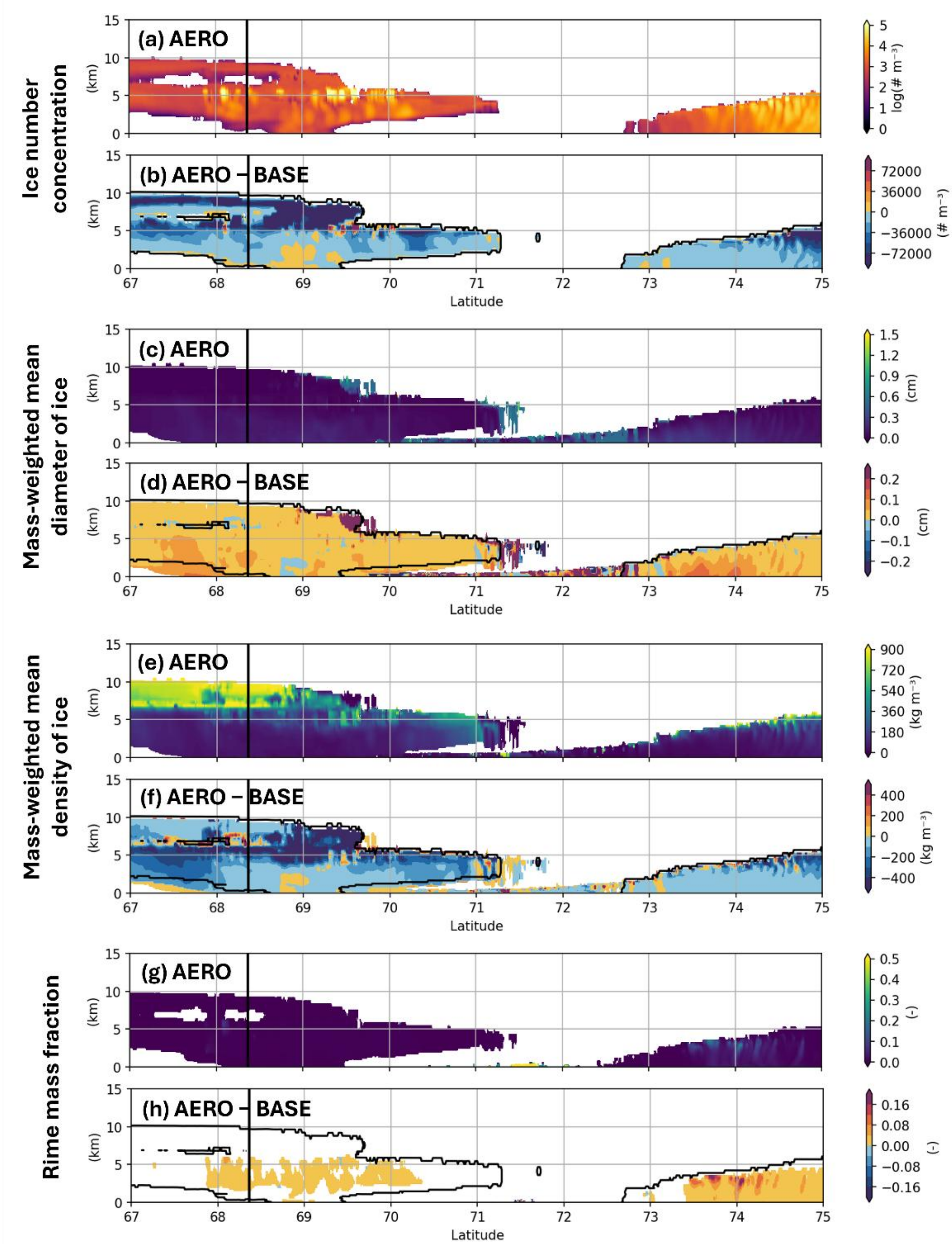

Figure 16. (a, c, e and g) AERO and (b, d, f and h) AERO – BASE along the EarthCARE pass on 00 UTC 20 Jan of (a–b) ice number concentration ($N_{i,tot}$; # m^{-3}), (c–d) mass-weighted mean diameter of ice ($D_{i,m}$; mm), (e–f) mass-weighted mean density of ice ($\rho_{i,m}$; kg m^{-3}) and (g–h) rime mass fraction ($F_{i,rim}$). The black line in (b, d, f and h) is where $N_{i,tot}$ is > 0 in BASE. The vertical black lines show the latitude of Inuvik.

https://doi.org/10.5194/egusphere-2026-4229
Preprint. Discussion started: 28 July 2026

4.4 Sensitivity to ice nucleation parameterization

We showed that the presence of supercooled liquid water in layered mixed-phase clouds in AERO compared to BASE occurs from differences in ice nucleation, which was changed from C86 (a temperature-dependent parameterization) in BASE to DM10 (an aerosol number-dependent parameterization) in AERO (Section 2.2). The sensitivity to the choice of ice nucleation parameterization is further analyzed here, based on the tests described in Table 2.

The percentage of heights in specific layers with liquid-containing clouds are shown in Figs. 17–18 for all simulations, except CAPS. Between 0 and 3 km altitude, CAPS has higher percentages of height distances covered by liquid clouds than in the 1-km simulations (not shown), especially over Alaska. Results among the 1-km simulations are similar, except in the northern part of the domain, where the percentage is slightly higher in BASE-DM10_Nai1, BASE-DM10_Nai2, AERO, AERO-DM10_Nai1 and AERO-DM10_Nai2. Nevertheless, the comparison among the 1-km simulation is interesting.

Using the DM10 parameterization for ice nucleation, with either a fixed $N_{a,i}$ (as in BASE-DM10_Nai1, BASE-DM10_Nai2, AERO-DM10_Nai1, and AERO-DM10_Nai2) or a variable $N_{a,i}$ (as in AERO), results in higher percentages of vertical levels covered by liquid-phase clouds in all layers, especially between 3–4 and 4–5 km altitude. Fig. 17e–p shows that as the fixed $N_{a,i}$ decreases from 15×10^6 to 15×10^4 # kg^{-1} in BASE-DM10 and in AERO-DM10, the percentage increases at altitudes above 3 km. Among simulations that employ the same ice nucleation scheme, the results are similar, i.e., between BASE and AERO-C86, between BASE-DM10_Nai1 and AERO-DM10_Nai1 and between BASE-DM10_Nai2 and AERO-DM10_Nai2. AERO-DM10_Nai1 and BASE-DM10_Nai1 yield results closest to AERO. Overall, the use of the $N_{a,i}$-dependent DM10 compared to C86 strongly influences the presence of liquid phase within the ice clouds. The use of an alternative ice nucleation scheme (Tobo et al., 2013) in AERO-T13 also produces a large amount of mixed-phase clouds in the simulation (Fig. 18u–x), but less than in AERO in the northeast part of the domain.

Along the EarthCARE track (Fig. 19), BASE-DM10_Nai1, AERO-DM10_Nai1, and AERO-T13 produce significant layered mixed-phase clouds in type A. The mixed-phase clouds in type A are simulated at slightly higher altitudes than in the satellite retrievals, except in AERO-T13, which correctly simulates a layer near 3 km altitude (between 68.5–69° latitude). Along the satellite pass, simulations using the same ice nucleation scheme show similar, but still somewhat different, results. For example, AERO-DM10_Nai1 simulates more mixed-phase clouds between 69.5 and 70.5° latitude (in type A) compared to BASE-DM10_Nai1, while producing similar overall results for the type B clouds.

In summary, the differences in the presence of mixed-phase clouds between simulations are primarily driven by the choice of ice nucleation parameterization. Replacing the temperature-dependent C86 parameterization used in BASE with the aerosol-dependent formulation of DM10 in AERO leads to a greater persistence of supercooled liquid water, especially above 3 km altitude. This is because the DM10 scheme, which depends on ice-nucleating aerosol concentrations, generally produces lower ice number concentrations than the C86 formulation, thereby reducing glaciation efficiency and allowing liquid water to remain in cloud layers, which in turn impacts the atmospheric state and radiative transfer. Sensitivity experiments further show that

https://doi.org/10.5194/egusphere-2026-4229
Preprint. Discussion started: 28 July 2026

decreasing $N_{a,i}$ concentrations enhance this effect, increasing the frequency of liquid-containing layers. Overall, the aerosol-aware ice nucleation schemes promote more extensive and vertically developed mixed-phase clouds than the original C86 temperature-based formulation, highlighting the critical role of ice nucleation in controlling cloud phase partitioning in a weather forecast model. This result agrees well literature showing that the amount of supercooled liquid water and the cloud phase structure in Arctic MPCs is very sensitive to the representation of ice microphysical processes and INPs in larger-scale models (e.g., Forbes and Ahlgrimm, 2014; Gjelsvik et al., 2025; Glassmeier et al., 2017; Sauerland et al., 2024; Zhao and Liu, 2022).

https://doi.org/10.5194/egusphere-2026-4229
Preprint. Discussion started: 28 July 2026

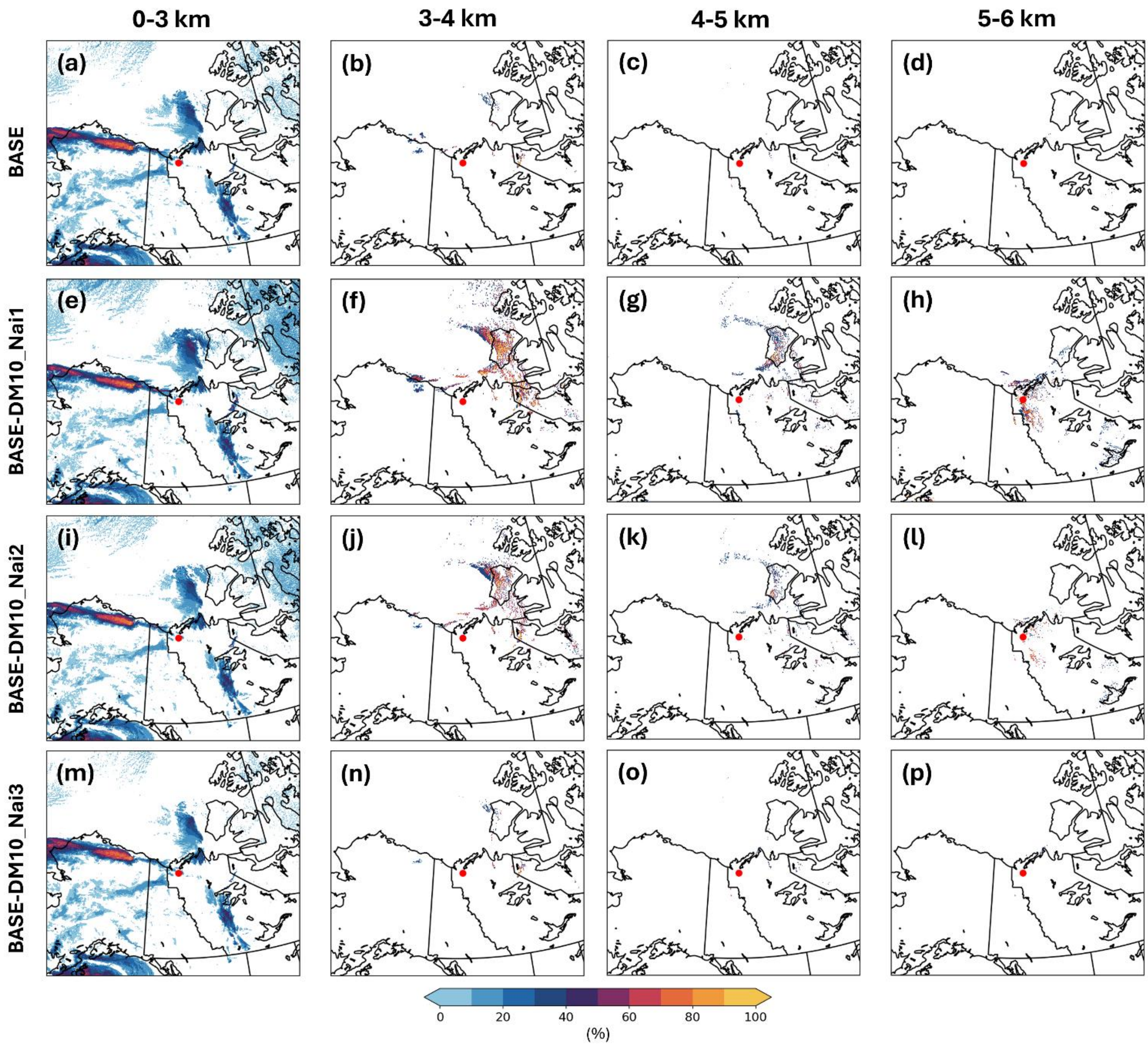

Figure 17. At 00 UTC 20 Jan 2026, percentage of layer height covered by liquid clouds for (a–d) BASE, (e–h) BASE-DM10_Nai1, (i–l) BASE-DM10_Nai2 and (m–p) BASE-DM10_Nai3 for the layers between heights of (a, e, i, and m) 0 and 3 km, (b, f, j and n) 3 and 4 km, (c, g, k and o) 4 and 5 km, and (d, h, l and p) 5 and 6 km.

https://doi.org/10.5194/egusphere-2026-4229
Preprint. Discussion started: 28 July 2026

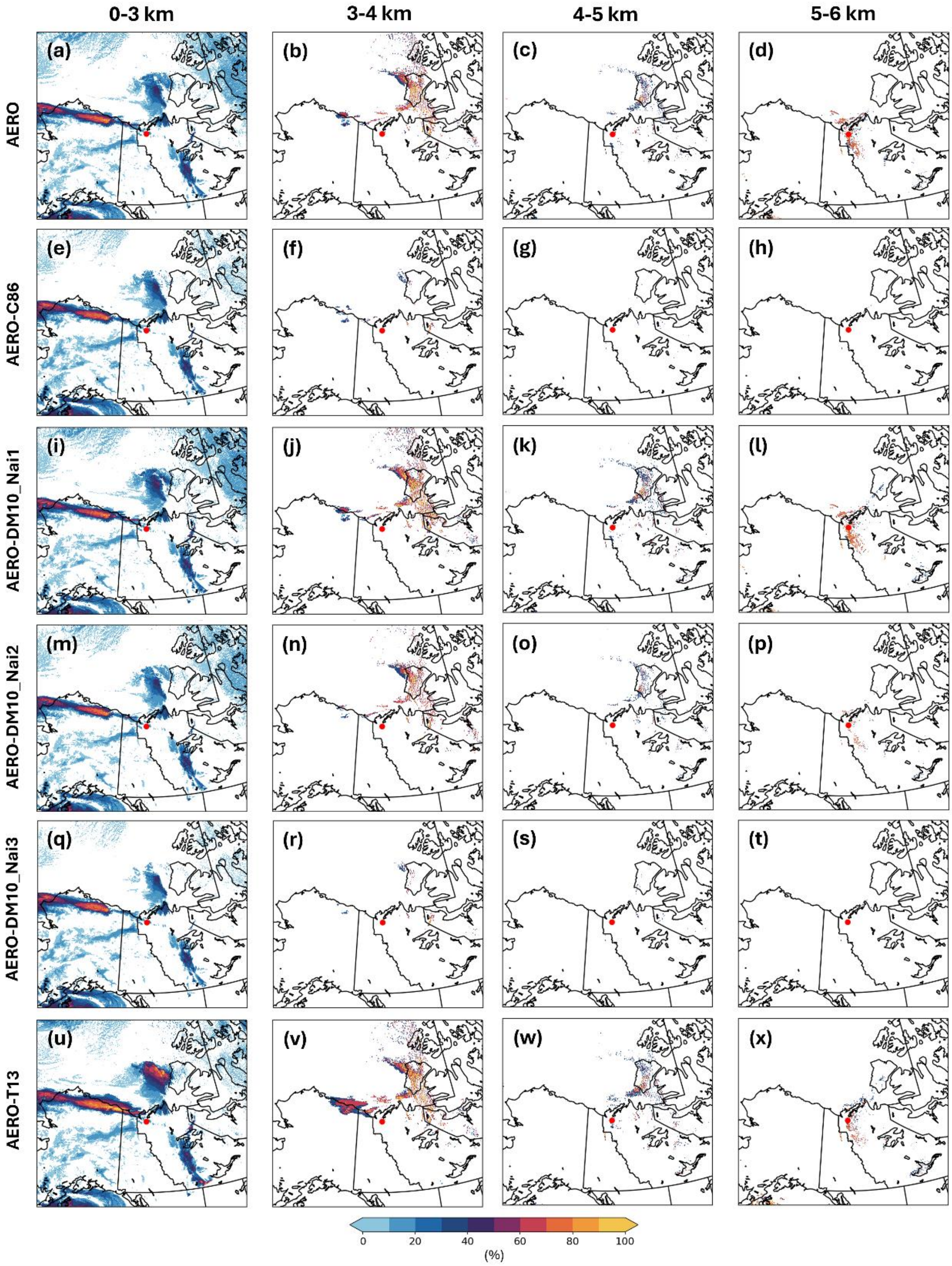

Figure 18. At 00 UTC 20 Jan 2026, percentage of layer height covered by liquid clouds for (a–d) AERO, (e–h) AERO-C86, (i–l) AERO-DM10_Nai1, (m–p) AERO-DM10_Nai2, (q–t) AERO-DM10_Nai3 and (u–x) AERO-T13 for the layers between heights of (a, e, i, m, q and u) 0 and 3 km, (b, f, j, n, r and v) 3 and 4 km, (c, g, k, o, s and w) 4 and 5 km, and (d, h, l, p, t and x) 5 and 6 km.

https://doi.org/10.5194/egusphere-2026-4229
Preprint. Discussion started: 28 July 2026

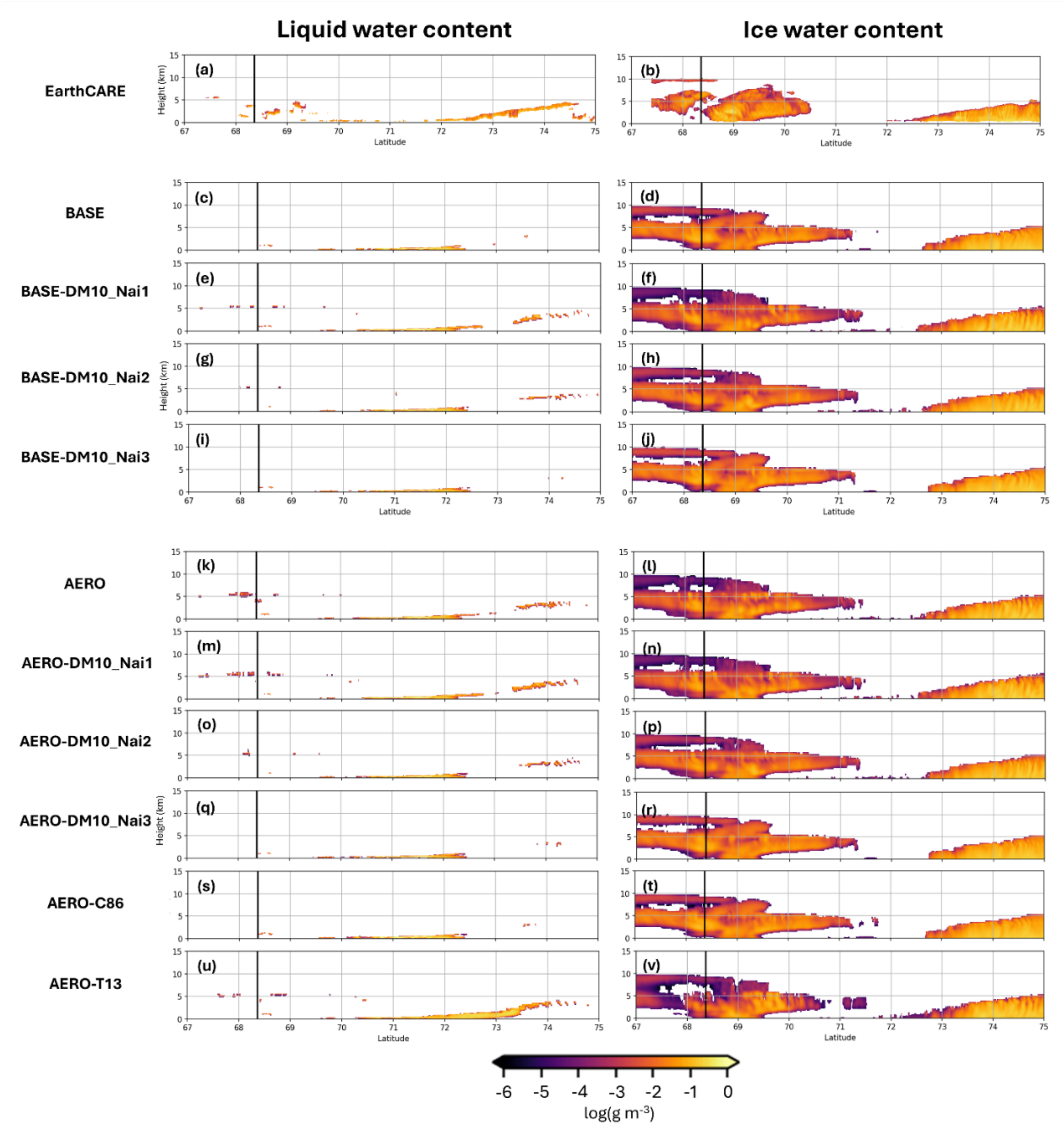

Figure 19. (a, c, e, g, i, k, m, o, q, s and u) liquid water content (g m^{-3}) and (b, d, f, h, j, l, n, p, r, t and v) ice water content (g m^{-3}) along the EarthCARE pass on 00 UTC 20 Jan for (a–b) EarthCARE retrievals, (c–d) BASE, (e–f) BASE-DM10_Nai1, (g–h) BASE-DM10_Nai2, (i–j) BASE-DM10_Nai3, (k–l) AERO, (m–n) AERO-DM10_Nai1, (o–p) AERO-DM10_Nai2, (q–r) AERO-DM10_Nai3, (s–t) AERO-C86 and (u–v) AERO-T13.

5. Conclusions and perspectives

This study introduces a prognostic treatment of aerosols in the P3 microphysics scheme used in GEM-based NWP systems at ECCC. The impacts are evaluated using high-resolution simulations of Arctic mixed-phase clouds for which a set of co-

https://doi.org/10.5194/egusphere-2026-4229
Preprint. Discussion started: 28 July 2026

located observational data is available during the PONEX campaign. Explicitly predicting both the water-friendly and the ice-friendly aerosol number mixing ratios enables a more physically consistent representation of aerosol-cloud interactions compared to the traditional P3 approach, which uses a fixed number of aerosols in time and space. As expected, the inclusion of prognostic aerosols does not substantially modify the large-scale cloud distribution and system since the synoptic-scale dynamics remain little changed. However, it strongly affects the cloud microphysics and the phase partitioning. The prognostic aerosol configuration produces fewer, but larger, ice particles, leading to enhanced reflectivity and increased riming. At the same time, it favors higher CWC and reduced IWC, resulting in more persistent supercooled liquid layers. The simulation with prognostic aerosols simulated warmer cloud-top temperatures and higher outgoing longwave radiation. Comparison along the EarthCARE satellite track shows that both configurations reproduce the general cloud structure, including the embedded generating cells, but the prognostic aerosol scheme better captures the characteristics of the layered mixed-phase clouds, particularly in the persistence and vertical structure of layers.

A key result of this study is the strong sensitivity to the ice nucleation parameterization. Aerosol-dependent schemes, such as DeMott et al. (2010) and Tobo et al. (2013), lead to reduced ice number concentrations and enhanced liquid water persistence compared to the temperature-dependent formulation of Cooper (1986), which is used by default in P3 in the absence of prognostic aerosols. Sensitivity experiments demonstrate that both the parameterization choice and the assumed ice-nucleating aerosol concentrations critically control cloud phase and the vertical structure of the embedded supercooled liquid layers. Other factors that may also have impacted the simulations of the layered mixed-phase clouds, such as the model vertical resolution and other microphysics processes (e.g., the Wegener-Bergeron-Findeisen process), were not explored in this study.

This analysis is also based primarily on a single Arctic MPCs case, which limits the generality of the conclusions. However, preliminary multi-case experiments over a larger set of winter simulations indicate qualitatively consistent impacts of prognostic aerosols supporting the robustness of the findings and this under two different GEM-based modelling frameworks: the 1-km simulations described in here (used daily during the entire PONEX campaign) and with the 2.5-km grid spacing HRDPS (not shown). The impacts of prognostic aerosols in P3 and in GEM-based operational high-resolution NWP systems of ECCC will be tested in the future for other weather conditions. The results suggest that explicitly predicting aerosol concentrations can meaningfully influence cloud and precipitation processes while requiring only minor modifications to the model configuration and a negligible increase in computational cost.

Finally, aerosol initialization relies on climatological fields and simplified emission assumptions, which may not fully represent real-time variability (Appendix B1). Future work should focus on improving aerosol initialization through the assimilation of observations or with using outputs from the Regional Air Quality Deterministic Prediction System (RAQDPS), and on extending the evaluation across different seasons and meteorological regimes. Further coupling with advanced chemistry modules and alternative aerosol parameterizations for the P3 aerosol aware code assessment in operational forecasting systems at coarser spatial scales will be essential to quantify the added value for NWP and climate applications.

https://doi.org/10.5194/egusphere-2026-4229
Preprint. Discussion started: 28 July 2026

Appendix A: Description of changes up to P3v5.5

The latest P3 version described in the scientific literature is v5.3 in Morrison et al. (2025), and references therein, in which the complete three-moment ice configuration was included. Since then, some changes, documented in the official P3 GitHub repository (https://github.com/P3-microphysics/P3-microphysics/), have been made to P3.

Most of the changes did not affect the microphysics solution, as they were minor bug fixes and/or optimization. Only the following two changes impacted the solution significantly relative to v5.3: (1) the inclusion of Hallett-Mossop (Hallett and Mossop, 1974) secondary ice production (HM-SIP) when using a single ice category (Cholette et al., 2024) and (2) a new method to compute the ice particle size distribution shape parameter in the complete three-moment ice configuration.

The HM-SIP was already included in versions prior to v5.5, but only when two or more ice categories (nCat) were used. The inclusion of this process for a single ice category is new and justified by the improvements in the freezing rain frequency bias index shown in Cholette et al. (2024). The HM-SIP process has been modified and tested with HRDPS precipitation-type statistics for 60 cases during winter 2022 as documented in the P3 GitHub repository. HM-SIP is relatively well quantified compared to other SIP mechanisms, with the production of ice splinters (with an assumed diameter of 10 μm) occurring between -3°C and -8°C from the accretion of large drops (rain) onto large, rimed ice particles. The process in P3 results in changes in cloud, rain and ice mass and ice number mixing ratios due to ice multiplication via rime-splintering. The minimum mass-weighted mean ice diameter for HM-SIP to occur in the P3 scheme differs between nCat=1 and nCat>1, based on differences in ice properties when dilution is considered for nCat>1. For nCat>1, $D_{i,m}$ must be greater than 1 mm whereas for nCat=1 it must be greater than 0.25 mm. An additional criterion is applied for HM-SIP with nCat=1 requiring that the lowest model level temperature be < 9°C. This is because HM-SIP with nCat=1 suppressed convection too much during the warmer seasons. For both nCat=1 or nCat>1, a minimum bulk rime fraction ($F_{i,rim}$) of 0.5 and a maximum bulk liquid fraction ($F_{i,liq}$) of 0.1 are required for HM-SIP, implying that the ice is partially to fully rimed (i.e., it represents rimed ice or graupel, not unrimed crystals) and completely or nearly completely frozen (dry) ice particles during the process. It is assumed that all accreted rain contributes to splintering, but accreted cloud water contributes to splintering only when nCat=1.

Two options for the 3-moment ice configuration exist in P3. The first option follows Milbrandt et al. (2021) and assumes that the shape parameter of the ice PSD (μ) remains constant during the following microphysical processes: cloud and rain collection, sublimation, shedding, melting and self-collection. The second option, described in Morrison et al. (2025), allows μ to change during all processes. A new method to compute μ when the 3-moment ice is employed has been incorporated into P3 v5.5. Instead of using iterations to solve for μ directly in the scheme, which can be expensive if a larger number of iterative steps is reached and depends on the interpolated value from the ice lookup table of the mass-weighted mean ice density as a function of the bulk state, the new method uses a new lookup table to obtain μ and $\rho_{i,m}$ from the set of prognostic variables. The two variables are interpolated from the new lookup table as a function of $Z_{i,tot}/q_{i,tot}$ (which has 80 indices), $q_{i,tot}/N_{i,tot}$ (which has 50 indices), $\rho_{i,rim}$ (which has 5 indices), $F_{i,rim}$ (which has 4 indices) and $F_{i,liq}$ (which has 4 indices). The results

https://doi.org/10.5194/egusphere-2026-4229
Preprint. Discussion started: 28 July 2026

using the two approaches are similar and are documented in the P3 GitHub repository (https://github.com/P3-microphysics/P3-microphysics/blob/main/test-summaries/20250505_v5.3.15_gem530a10_W22_S22_OPT_3MOM_LF.pdf).

Appendix B: Code description of prognostic aerosols in P3

The code for the implementation of prognostic aerosols in P3 v6.0 follows Thompson and Eidhammer (2014) and the use of prognostic aerosols in the code is optional: the solution reverts back to v5.5 if prognostic aerosols are not used.

B1 Aerosols initialization and surface emissions ($\mathbf{N_{a,w\,sfc\_emission}}$, $\mathbf{N_{a,i\,sfc\_emission}}$)

The aerosols number mixing ratios are initialized with linear interpolation in time to the date of the start of the model run, from monthly means derived from multiyear (2001–2007) global model simulations with 0.5° longitude and 1.25° latitude spacing (Colarco et al., 2010). Monthly mean aerosol fields derived from 2001–2007 observations provide a reasonable representation of the climatological Arctic aerosol distribution; however, long-term observations indicate substantial changes in Arctic aerosol loading and composition since the early 2000s, including declining sulfate and black carbon concentrations associated with reductions in anthropogenic emissions (Breider et al., 2017), alongside an increasing influence of episodic biomass-burning emissions that can substantially perturb Arctic aerosol properties and concentrations (Gramlich et al., 2024). Consequently, the prescribed aerosol fields should be interpreted as a historical climatology rather than a representation of present-day Arctic conditions. In these global simulations, particles and their precursors are emitted by natural and anthropogenic sources and simulated with size bins for multiple species of aerosols (sulfates, sea salts, organic carbon, dust and black carbon) using the Goddard Chemistry Aerosol Radiation and Transport (GOCART) model of Ginoux et al. (2001). The dust mass larger than 0.5 µm is assumed to be the ice-nucleating, non-hygroscopic, mineral dust mode input for N_{ifa}. All other species, except black carbon, are combined to be an internally mixed cloud droplet-nucleating, hygroscopic, CCN input for N_{wfa}. Inputs are number mixing ratios converted from mass mixing ratio assuming lognormal distributions (Chin et al., 2002).

After being initialized, $N_{a,w}$ and $N_{a,i}$ evolve in time and space following Eqs. (2–4), except for the lowest model level ($N_{a,w}(k_{bot})$ and $N_{a,i}(k_{bot})$) which accounts for surface emissions at every step. As mentioned before, the values of $N_{a,w}(k_{bot})$ (i.e., at the lowest model level) increased too rapidly and, thus, diverged from the climatology, when the Thompson and Eidhammer (2014) approach for surface emission was used. Therefore, surface emission for both $N_{a,w}(k_{bot})$ and $N_{a,i}(k_{bot})$ use a relaxation back to the climatology assuming a timescale of 1.5 h. Therefore, $N_{a,w\,sfc\_emission} = 0.000185\,(N_{wfa} - N_{a,w}(k_{bot}))$ and $N_{a,i\,sfc\_emission} = 0.000185\,(N_{ifa} - N_{a,i}(k_{bot}))$.

https://doi.org/10.5194/egusphere-2026-4229
Preprint. Discussion started: 28 July 2026

B2 Cloud droplet nucleation ($N_{c,nuc}$)

Cloud droplets nucleate from the explicit aerosol number mixing ratio ($N_{a,w}$), limited to conditions with water supersaturation higher than 0.0001%.

$$N_{c,nuc} = \max(\frac{N_{act}-N_c}{\Delta t}, 0) \quad \text{(B1)}$$

In Eq. (B1), $N_{act} = \min(N_{a,w}, N_c')$ and N_c' is the number of activated cloud condensation nuclei. Two parameterizations for N_c' are tested and both use the following formula:

$$N_c' = \frac{N_{a,w}}{2}[1 - \mathrm{erf}(u)] \quad \text{(B2)}$$

where erf is the Gaussian error function and u is given by Eq. (B3).

The parameterization of Khvorostyanov and Curry (2005) (hereafter referred to KC) based on water supersaturation and the parameterization of Abdul-Razzak and Ghan (2000) (hereafter referred to ARG) based on vertical motion has been compared. Both parameterizations give similar results in our tests (not shown). The parameterization of ARG is employed by default with prognostic aerosols in P3 while KC is employed in the baseline configuration (i.e., without prognostic aerosols). Both the KC and ARG parameterizations use Eqs. (B3–B5):

$$u = \frac{2\log(\frac{s_0}{s_x})}{4.242\log(\sigma_i)} \quad \text{(B3)}$$

$$s_0 = \frac{2}{b^{0.5}}\left(\frac{A}{3r_m}\right)^{1.5} \quad \text{(B4)}$$

$$A = \frac{2\,m_w}{\rho_w R\,T}\left(0.0761 - 0.000155\,(T - 273.15)\right);\ b = \frac{v_i\,\varphi_m \varepsilon_m\,m_w\,\rho_s}{m_s \rho_w} \quad \text{(B5a–b)}$$

Here $\sigma_i = 2$ for KC and 1.8 for ARG, $r_m = 0.05\ \mu m$ for KC and $0.04\ \mu m$ for ARG, expressed in m and being the mean radius of aerosol (assuming the soluble material is ammonium sulphate), m_w is molar mass of water (0.018 kg mol^{-1}), ρ_w is the density of water (1000 kg m^{-3}), R is the gas universal constant (8.3187 J mol^{-1} kg^{-1}), T is air temperature (in K), v_i is the number of ions in the solution (i.e., 3), φ_m is the osmotic potential (i.e., 1), ε_m is the volume fraction of 0.9, ρ_s is the density (1777 kg m^{-3}) and m_s is the molecular weight (0.132 kg mol^{-1}) of the soluble fraction.

In KC and in Eq. (7), s_x is the water supersaturation ($q_v/q_{v,sat} - 1$) while in ARG s_x is given by s_{max}:

$$s_{max} = \left\{\sum_{i=1}^{I}\frac{1}{s_0^2}\left[f_i(\frac{\varsigma}{\eta_i})^{3/2} + g_i(\frac{s_0^2}{\eta_i+3\varsigma})^{3/4}\right]\right\}^{1/2} \quad \text{(B6)}$$

$$f_i \equiv 0.5\exp\left(2.5\log^2(\sigma_i)\right);\ g_i \equiv 1 + 0.25\log(\sigma_i) \quad \text{(B7a–b)}$$

$$\varsigma \equiv \frac{2A}{3}\left(\frac{\alpha W}{G}\right)^{\frac{1}{2}};\ \eta_i = \frac{(\alpha W/G)^{3/2}}{2\pi\rho_w\gamma\,N_{a,w}} \quad \text{(B8a–b)}$$

$$\alpha = \frac{g\,m_w\,L_v}{c_p\,R\,T^2} - \frac{g\,m_s}{R\,T};\ G = \frac{1}{\frac{\rho_w\,R\,T}{e_{sat}\,D_v\,m_w} + \frac{L_v\,\rho_w}{K_a\,T}\left(\frac{L_v\,m_w}{R\,T} - 1\right)};\ \gamma = \frac{R\,T}{e_{sat}\,m_w} + \frac{m_w\,L_v^2}{c_p\,p\,m_s\,T} \quad \text{(B9a–c)}$$

where q_v is water vapor mixing ratio, $q_{v,sat}$ is the water vapor saturated mixing ratio, e_{sat} water vapor saturated pressure, g is the gravitational acceleration constant (9.816 m s^{-2}), L_v is latent heat of vaporization (2501035 J kg^{-1}), c_p is specific heat

https://doi.org/10.5194/egusphere-2026-4229
Preprint. Discussion started: 28 July 2026

capacity (1005 J kg^{-1} K^{-1}), p is air pressure (in Pa), D_v is molecular diffusivity of water vapor in air ($8.794\ x\ 10^{-5}\frac{T^{1.81}}{p}$; in m^2 s^{-1}) and K_a [W m^{-1} K^{-1}] is thermal conductivity of air ($1.414\ x\ 10^{3}\ \mu_{air}$ where μ_{air} is dynamic viscosity of air $1.496\ x\ 10^{-6}\frac{T^{3/2}}{T+120}$). W is the vertical motion used to compute activation, taken as the sum of the grid-scale vertical motion (w) and the vertical motion derived from the subgrid-scale turbulent kinetic energy (TKE) assuming isotropic turbulence with a minimum set to 0.1 m s^{-1}: $W = \min\left(0.1, w + \left({}^{2}/_{3}\,TKE\right)^{\frac{1}{2}}\right)$. As before the implementation of prognostic aerosols, $N_{c,nuc}$ and $q_{c,nuc}$ are source terms for N_c and q_c, respectively, and $q_{c,nuc}$ is also a sink term for q_v.

B3 Ice nucleation ($N_{i,nuc}$)

The primary ice nucleation in P3 follows Eq. (B10) when the temperature is < -15°C and the supersaturation with respect to ice ($s_i = q_v/q_{v,sat,i} - 1$) is > 5%:

$$N_{i,nuc} = \max\left(\frac{N_{act,i} - \sum_{nCat} N_{i,tot}}{\Delta t}, 0\right) \quad \text{(B10)}$$

In Eq. (B10), $N_{act,i}$ follows C86 for the baseline P3 (Eq. B11) and DM10 with prognostic aerosols (Eq. B12):

$$N_{act,i\ C86} = a \exp[b(273.15 - T)]\left(\frac{1000}{\rho_{air}}\right) \quad \text{(B11)}$$

$$N_{act,i\ DM10} = a\ (273.16 - T)^b\ N_{a,i}{}^{c(273.16-T)+d}\left(\frac{1000}{\rho_{air}}\right) \quad \text{(B12)}$$

In Eq. (B11), a = 0.005 and b = 0.304. In Eq. (B12), a = 0.0000594, b = 3.33, c = 0.0264, d = 0.0033.

Another ice nucleation parameterization has been implemented in P3 and tested in this study following T13:

$$N_{act,i\ T13} = a\ e^{b(273.16-T)-11.6)}\ N_{a,i}{}^{c(273.16-T)+d}\left(\frac{1000}{\rho_{air}}\right) \quad \text{(B13)}$$

In Eq. (B13), a = 1, b = 0.46, c = 0 and d = 1.25. The nucleation sink term for T13 is given by

$$N_{i,nuc} = \max\left(\frac{0.5(X+abs(X))}{\Delta t}, 0\right);\ X = N_{act,i} - \sum_{nCat}(N_{i,tot} - (N_{r,het} + N_{c,het})dt) \quad \text{(B14a,b)}$$

with $N_{r,het}$ and $N_{c,het}$ being the heterogenous freezing of rain drops and cloud droplets as computed in the baseline P3 following MM15. The factor $\left(\frac{1000}{\rho_{air}}\right)$ in Eqs. (B11–B13) is to convert from L^{-1} to kg^{-1}. As before the implementation of prognostic aerosols, $N_{i,nuc}$ and $q_{i,nuc}$ are source terms for $N_{i,tot}$ and $q_{i,tot}$, respectively, and $q_{i,nuc}$ is also a sink term for q_v.

B4 Cloud and rain evaporation ($N_{c,evp}$, $N_{r,evp}$)

As mentioned before, in the baseline P3, there is no cloud number mixing ratio tendency for cloud evaporation (only a mass mixing ratio tendency was included). With prognostic aerosols, $N_{c,evp}$ is a new term. It is assumed to be proportional to the changes in q_c from the evaporated mass ($q_{c,evp}$):

$$N_{c,evp} = q_{c,evp}\frac{N_c}{q_c} \quad \text{(B15)}$$

https://doi.org/10.5194/egusphere-2026-4229
Preprint. Discussion started: 28 July 2026

with $q_{c,evp}$ is given by Eq. (C6) of MM15.

Rain evaporation either with and without prognostic aerosols is given by $N_{r,evp} = q_{r,evp}\frac{N_r}{q_r}$. The condensation/evaporation rate of rain follows the same approach as cloud condensation/evaporation to yield an expression similar to $q_{c,evp}$ except that the time relaxation scale (τ) is for rain in Eq. (C6) of MM15. As before the implementation of prognostic aerosols, $N_{c,evp}$ and $N_{r,evp}$ are sink terms for N_c and N_r, and $q_{c,evp}$ and $q_{r,evp}$ sink terms for q_c and q_r, respectively. $q_{c,evp}$ and $q_{r,evp}$ are also source terms for q_v.

B5 Sublimation ($N_{i,sub}$) of ice and evaporation of mixed-phase particles ($N_{l,evp}$)

Deposition/sublimation of ice occurs when the liquid fraction is 0. If the liquid fraction is greater than 0, this process is considered as condensation/evaporation of the liquid water in mixed-phase particles. The calculation of deposition/sublimation is described in MM15 (Eq. C7) and the mixed-phase particle condensation/evaporation is given by Eq. (A6) in Cholette et al. (2019). $N_{i,sub}$ and $N_{l,evp}$ are sink terms for $N_{i,tot}$, while $q_{i,sub}$ is a sink term for $q_{i,tot}$ as well as for $q_{i,rim}$, $B_{i,rim}$ and $q_{i,dep}$. $q_{l,evp}$ is a sink term for $q_{i,liq}$, and, along with $q_{i,sub}$, a source term for q_v.

B6 Rain collecting aerosols ($N_{r,wsca}$, $N_{r,isca}$)

Aerosols are removed by precipitation scavenging using aerosol collision efficiencies computed as in (Wang et al., 2010) using a standard geometric sweep-out.

$$N_{r,wsca} = \Lambda N_{a,w} \tag{B16}$$

$$\Lambda = \int_0^{\infty} \frac{\pi}{4}(D_r + D_a)^2 \left(V(D_r) - V(D_a)\right) E(D_r, D_a) N_r(D_r) dD_r \tag{B17}$$

D_r and D_a denote the raindrop and aerosols diameters, respectively, $N_r(D_r)$ is the raindrop size distribution, and $V(D_r)$ and $V(D_a)$ are the terminal velocities of raindrop and aerosol particles, respectively. $E(D_r, D_a)$ is the raindrop-aerosols collection efficiency, which represents the ratio of the total number of collisions occurring between a raindrop and an aerosol to the total number of particles in an aera equal to the raindrop's effective cross-section area as calculated in (Slinn and Shen, 1970). Assuming $D_a << D_r$ and $V(D_a) << V(D_r)$, then

$$N_{r,wsca} = N_{a,w} \int_0^{\infty} \frac{\pi}{4} {D_r}^2 V(D_r) E(D_r, D_a) N_r(D_r) dD_r \tag{B18}$$

$$N_{r,isca} = N_{a,i} \int_0^{\infty} \frac{\pi}{4} {D_r}^2 V(D_r) E(D_r, D_a) N_r(D_r) dD_r \tag{B19}$$

and the collection efficiency is given by

$$E(D_r, D_a) = \frac{4}{Re\, Sc}\left[1 + 0.4\, Re^{\frac{1}{2}} Sc^{\frac{1}{3}} + 0.16\, Re^{\frac{1}{2}} Sc^{\frac{1}{2}}\right] + \frac{4D_a}{D_r}\left[0.02 + \frac{D_a}{D_r}\left(1 + 2\, Re^{\frac{1}{2}}\right)\right] + \left(\frac{St - St^*}{St - St^* + {}^2/_3}\right)^{3/2} \tag{B20}$$

with $Re = \frac{D_r V(D_r)\rho_{air}}{2\mu_{air}}$, $Sc = \frac{\mu_{air}}{\rho_{air} D_{diff}}$, $D_{diff} = \frac{k_b T C_c}{3\pi\mu_{air} D_a}$, $St = \frac{2(\rho_a - \rho_{air}) D_a^2 C_c (V(D_r) - V(D_a))}{18\mu_{air} D_r}$, $St^* = \frac{1.2 + \frac{1}{12}\ln(1+Re)}{1 + \ln(1+Re)}$ and $C_c = 1 + \frac{2\lambda}{D_a}(1.257 + 0.4\exp(-0.55\frac{D_a}{\lambda}))$. For simplicity and to avoid an increase in computational cost, $E(D_r, D_a)$ is computed

https://doi.org/10.5194/egusphere-2026-4229
Preprint. Discussion started: 28 July 2026

with the bulk mean-volume diameter of rain ($D_r = D_{r,m} = \left(\frac{6\, q_r}{\pi \rho_w N_r}\right)^{1/3}$) and assuming that D_a is 0.04 µm and 0.8 µm for $N_{r,wsca}$ and $N_{r,isca}$, respectively and that $V(D_a)$ is negligible. $N_{r,wsca}$ and $N_{r,isca}$ are sink terms for the number mixing ratios of aerosols and do not change the number mixing ratio tendencies of the collector hydrometeors (i.e., rain).

B7 Ice collecting aerosols ($\mathbf{N_{i,wsca}}$, $\mathbf{N_{i,isca}}$)

Similarly to Eqs. (B18–19), aerosols collected by ice are given by

$$N_{i,wsca} = N_{a,w} \int_0^\infty A(D)\, V(D)\; E(D, D_a)\, N(D) dD \tag{B21}$$

$$N_{i,isca} = N_{a,i} \int_0^\infty A(D)\, V(D)\; E(D, D_a)\, N(D) dD \tag{B22}$$

with $A(D)$ and $V(D)$ being the projected area and terminal velocity relationships as a function of the ice particle diameter (D) (Eqs. (12–13) in Cholette et al. (2019), respectively). Note that for ice in P3, these relationships are given by the 4 regimes (i.e., small spherical ice, unrimed non-spherical ice crystals, partially rimed non-spherical ice crystals, and completely rimed spherical ice crystals) of the ice size distribution $N(D)$ represented by a gamma function (Cholette et al., 2019; MM15). $E(D, D_a)$ is given by Eq. (B20), but when replacing the rain terminal velocity and diameter with those of the ice particles. Also, since the rates are computed offline and stored in a lookup table as a function of the state variables ($q_{i,tot}/N_{i,tot}$, $\rho_{i,rim}$, $F_{i,rim}$ and $F_{i,liq}$), it is assumed that the air temperature is -20°C in the calculation of $E(D, D_a)$. Then the rates are interpolated between the state variables during the integration time. $N_{i,wsca}$ and $N_{i,isca}$ are sink terms for the number mixing ratios of aerosols and do not change the number mixing ratio tendencies of the collector hydrometeors (i.e., ice).

B8 Homogeneous freezing of aqueous aerosols ($\mathbf{N_{aw,hom}}$, $\mathbf{q_{aw,hom}}$)

As in Thompson and Eidhammer (2014), the homogeneous freezing of deliquesced aerosols based on the hygroscopic aerosols concentration is parameterized following (Koop et al., 2000). It occurs for temperatures colder than -35°C and supersaturations with respect to ice ($s_i = q_v/q_{v,sat,i} - 1$) higher than 40%.

$$N_{aw,hom} = N_{a,w}[1 - \exp(-J_{rate}\, Vol_{aerosols} dt)] \tag{B23}$$

Here, $Vol_{aerosols} = \frac{4\pi}{3} {r_m}^3$ and J_{rate} is the probability of freezing given by

$$J_{rate} = 10^{-906.7+8502\, \Delta a_w - 26924\, \Delta {a_w}^2 + 29180\, \Delta {a_w}^3} \tag{B24}$$

$$\Delta a_w = \frac{q_v}{q_{v,sat}} - a_w^i \tag{B25}$$

$$a_w^i = \exp\left(\frac{210368 + 131.438\, T - \frac{3323730}{T} - 41729.1 \log(T)}{R\, T}\right) \tag{B26}$$

with T being the temperature, R the universal gas constant, q_v the water vapor mixing ratio and $q_{v,sat}$ the water vapor mixing ratio at saturation. $N_{aw,hom}$ is a sink term for $N_{a,w}$ and a source term for $N_{i,tot}$. As for other freezing processes in P3, it is

https://doi.org/10.5194/egusphere-2026-4229
Preprint. Discussion started: 28 July 2026

725 assumed that dense ice (with a rime density of 900 kg m^{-3}) is created from this process ($q_{aw,hom}$; Eq. B27). The change in ice
726 mass from homogeneous freezing of aerosols is

727 $$q_{aw,hom} = \frac{4\pi}{3}\rho_{frz} D_{frz}^3 N_{aw,hom} \quad \text{(B27)}$$

728 where $D_{frz} = 1\ \mu m$ and $\rho_{frz} = 900$ kg m^{-3}. $q_{aw,hom}$ is a source term for $q_{i,tot}$ and $q_{i,rim}$, a sink term for q_v, and it also affects
729 temperature via latent heating.

730 **Appendix C: List of variables**

List of variables in the main text		
Variable name	Description	Units
$A(D)$	Projected area-diameter relation	m^2
$B_{i,rim}$	Rime volume mixing ratio	m^3 kg^{-1}
CWC	Cloud water content	g m^{-3}
D	Particle diameter	m
$D_{c,m}$	Mass-weighted mean diameter of cloud	m
$D_{i,m}$	Mass-weighted mean diameter of ice	m
$F_{i,liq}$	Bulk liquid mass fraction	-
$F_{i,rim}$	Bulk rime mass fraction	-
IWC	Ice water content	g m^{-3}
λ_c	Slope parameter of cloud PSD	m^{-1}
$m(D)$	Mass-diameter relation	kg
$N_{a,w}$	Number mixing ratio of water-friendly aerosols	# kg^{-1}
$N_{a,i}$	Number mixing ratio of ice-friendly aerosols	# kg^{-1}
$N_{aw,hom}$	Number mixing ratio change due to homogeneous freezing of $N_{a,w}$	# kg^{-1} s^{-1}
$N_{a,i\ sfc\_emission}$	Lowest model level emission of ice-friendly aerosols	# kg^{-1} s^{-1}
$N_{a,w\ sfc\_emission}$	Lowest model level emission of water-friendly aerosols	# kg^{-1} s^{-1}
N_c	Cloud number mixing ratio	# kg^{-1}
$N_{c,evp}$	Number mixing ratio change due to cloud evaporation	# kg^{-1} s^{-1}
$N_{c,nuc}$	Number mixing ratio change due to cloud nucleation	# kg^{-1} s^{-1}
$N(D)$	Ice particle size distribution	# kg^{-1} m^{-1}
$N_{i,nuc}$	Number mixing ratio change due to ice nucleation	# kg^{-1} s^{-1}
$N_{i,sub}$	Number mixing ratio change due to ice sublimation	# kg^{-1} s^{-1}
$N_{i,tot}$	Ice number mixing ratio	# kg^{-1}
$N_{i,isca}$	Number mixing ratio change due to ice collecting ice-friendly aerosol	# kg^{-1} s^{-1}
$N_{i,wsca}$	Number mixing ratio change due to ice collecting water-friendly aerosol	# kg^{-1} s^{-1}
$N_{l.evp}$	Number mixing ratio change due to liquid evaporation of mixed-phase particles	# kg^{-1} s^{-1}
N_r	Rain number mixing ratio	# kg^{-1}
$N_{r.evp}$	Number mixing ratio change due to rain evaporation	# kg^{-1} s^{-1}
$N_{r,isca}$	Number mixing ratio change due to rain collecting ice-friendly aerosol	# kg^{-1} s^{-1}
$N_{r,wsca}$	Number mixing ratio change due to rain collecting water-friendly aerosol	# kg^{-1} s^{-1}
q_c	Cloud mass mixing ratio	kg kg^{-1}
$q_{i,dep}$	Ice mass mixing ratio from vapor growth	kg kg^{-1}
$q_{i,liq}$	Liquid in ice mass mixing ratio	kg kg^{-1}
$q_{i,rim}$	Rime ice mass mixing ratio	kg kg^{-1}
$q_{i,tot}$	Total ice mass mixing ratio	kg kg^{-1}

https://doi.org/10.5194/egusphere-2026-4229
Preprint. Discussion started: 28 July 2026

q_r	Rain mass mixing ratio	kg kg^{-1}
ρ_{air}	Air density	kg m^{-3}
$\rho_{i,m}$	Mass-weighted mean density of ice	kg m^{-3}
$r_{eff,c}$	Cloud effective radius	m
$r_{eff,i}$	Ice effective radius	m
RH_i	Relative humidity with respect to ice	%
RH_w	Relative humidity with respect to water	%
t	time	s
T	Air temperature	K
U	3D wind speed	m s^{-1}
μ_c	Shape parameter of the cloud size distribution	-
$V(D)$	Fall speed-diameter relation	m s^{-1}
V_X	Weighted fall speed	m s^{-1}
z	height	m
$Z_{i,tot}$	6-moment of the ice PSD	m^6 kg^{-1}

731

List of variables in Appendix A and B		
Variable name	Description	Units
C_c	Cunningham correction factor	-
c_p	Specific heat capacity	J kg^{-1} K^{-1}
D_a	Aerosol diameter	m
D_{diff}	Aerosol Brownian diffusivity coefficient	m^2 s^{-1}
D_{frz}	Diameter of $N_{a,w}$ homogeneous freezing	m
D_r	Raindrop diameter	m
D_v	Molecular diffusivity of water vapor in air	m^2 s^{-1}
Δt	Time step	s
ε_m	Volume fraction	-
$E(D_r, D_a)$	Collection efficiency between raindrop and aerosol	-
ε_m	Volume fraction	-
e_{sat}	Saturated water vapor pressure	Pa
g	Gravitational acceleration constant	m s^{-2}
K_a	Thermal conductivity of air	W m^{-1} K^{-1}
k_b	Boltzmann constant	J K^{-1}
λ	Mean free path of air molecules	m
L_v	Latent heat of vaporization	J kg^{-1}
m_s	Molecular weight of the soluble fraction	kg mol^{-1}
m_w	Molecular weight of water	kg mol^{-1}
N_{act}	Number of activated cloud nuclei	# kg^{-1}
$N_{act,i}$	Number of activated ice nuclei	# kg^{-1}
N_{ifa}	Number mixing ratio of ice-friendly aerosols from climatology	# kg^{-1}
N_{wfa}	Number mixing ratio of water-friendly aerosols from climatology	# kg^{-1}
N_c'	Number of activated cloud nuclei	# kg^{-1}
$N_r(D_r)$	Size particle distribution of rain	# kg^{-1} m^{-1}
φ_m	Osmotic potential	-
p	Air pressure	Pa
ρ_a	Density of aerosol	kg m^{-3}
ρ_{frz}	Density of $N_{a,w}$ homogeneous freezing	kg m^{-3}
ρ_w	Density of water	kg m^{-3}
ρ_s	Density of the soluble fraction	kg m^{-3}
$q_{aw,hom}$	Mass mixing ratio change due to $N_{a,w}$ homogeneous freezing	kg kg^{-1} s^{-1}
$q_{c.evp}$	Mass mixing ratio change due to cloud evaporation	kg kg^{-1} s^{-1}

$q_{c.nuc}$	Mass mixing ratio change due to cloud nucleation	kg kg^{-1} s^{-1}
$q_{i.nuc}$	Mass mixing ratio change due to ice nucleation	kg kg^{-1} s^{-1}
$q_{i.sub}$	Mass mixing ratio change due to ice sublimation	kg kg^{-1} s^{-1}
$q_{l.evp}$	Mass mixing ratio change due to liquid evaporation of mixed-phase particles	kg kg^{-1} s^{-1}
$q_{r.evp}$	Mass mixing ratio change due to rain evaporation	kg kg^{-1} s^{-1}
q_v	Vapor mass mixing ratio	kg kg^{-1}
$q_{v,sat}$	Saturated water vapor mass mixing ratio	kg kg^{-1}
$q_{v,sat,i}$	Saturated water vapor mass mixing ratio with respect to ice	kg kg^{-1}
R	Universal gas constant	J mol^{-1} kg-1
Re	Raindrop Reynold number	-
r_m	Geometric mean (modal) aerosol radius	m
Sc	Aerosol Schmidt number	-
St	Aerosol Stokes number	-
St^*	Critical Stokes number of aerosol	-
s_i	Supersaturation with respect to ice	-
σ_i	Geometric standard deviation of aerosol size distribution	-
s_{max}	Maximum supersaturation with respect to water	-
s_x	Supersaturation with respect to water	-
τ	Relaxation time scale	s
TKE	Turbulent kinetic energy	J kg^{-1}
μ	Shape parameter of ice PSD	-
μ_{air}	Dynamic viscosity of air	kg m^{-1} s^{-1}
$V(D_a)$	Terminal velocity of aerosol	m s^{-1}
$V(D_r)$	Terminal velocity of raindrops	m s^{-1}
v_i	Number of ions in the solution	#
w	Vertical velocity from boundary layer TKE	m s^{-1}
W	Grid-mean vertical velocity	m s^{-1}

Code, data, or code and data availability

The P3 code, which will also be available at https://github.com/P3-microphysics/P3-microphysics when accepted for publication, the model settings files and the simulated outputs files for both BASE and AERO are available in Zenodo at https://doi.org/10.5281/zenodo.21169210 (Cholette, 2026). The GEM model code is available at https://github.com/ECCC-ASTD-MRD/gem with P3 interface files available at https://github.com/P3-microphysics/P3-microphysics/tree/main/interfaces/gem. The GOES data are available here: https://registry.opendata.aws/noaa-goes. The EarthCARE data can be downloaded here: https://portal.maap.eo.esa.int/earthcare/. The ECCC's surface site data at Inuvik (WXT536, MRR-PRO and the soundings) will be released soon or, if not prior the publication, the subset used will added on Zenodo (Cholette, 2026).

Author contributions

M. Cholette implemented the P3 code changes, developed and operated the 1-km simulations for PONEX, conducted the results analysis and principal contributor of the manuscript. C. Jouan, J. Milbrandt and H. Morrison helped implemented the

https://doi.org/10.5194/egusphere-2026-4229
Preprint. Discussion started: 28 July 2026

prognostic aerosols in P3 and GEM. Z. Qu, Z. Dedekind and Z. Mariani provided the various datasets used in this study and helped with their interpretations and associated figures. All co-authors edited the manuscript.

Competing interests

The authors declare no conflicts of interest.

Disclaimer

No disclaimer.

Acknowledgements

The authors would like to acknowledge the PONEX science team and their work in planning, preparing and operating the Polar Night Experiment that took place in January 2026 in Northwest Territories known as the Inuvialuit Settlement Region.

Financial support

Funding for the PONEX campaign was provided in part by the Canadian Space Agency.

References

Abdul-Razzak, H. and Ghan, S. J.: A parameterization of aerosol activation: 2. Multiple aerosol types, J. Geophys. Res. Atmospheres, 105, 6837–6844, https://doi.org/10.1029/1999JD901161, 2000.

Albrecht, B. A.: Aerosols, Cloud Microphysics, and Fractional Cloudiness, Science, 245, 1227–1230, https://doi.org/DOI: 10.1126/science.245.4923.1227, 1989.

Bélair, S., Crevier, L.-P., Mailhot, J., Bilodeau, B., and Delage, Y.: Operational Implementation of the ISBA Land Surface Scheme in the Canadian Regional Weather Forecast Model. Part I: Warm Season Results, J. Hydrometeorol., 4, 352–370, https://doi.org/10.1175/1525-7541(2003)4<352:OIOTIL>2.0.CO;2, 2003.

Bélair, S., Mailhot, J., Girard, C., and Vaillancourt, P.: Boundary Layer and Shallow Cumulus Clouds in a Medium-Range Forecast of a Large-Scale Weather System, Mon. Weather Rev., 133, 1938–1960, https://doi.org/10.1175/MWR2958.1, 2005.

de Boer, G., Morrison, H., Shupe, M. D., and Hildner, R.: Evidence of liquid dependent ice nucleation in high-latitude stratiform clouds from surface remote sensors, Geophys. Res. Lett., 38, https://doi.org/10.1029/2010GL046016, 2011.

Breider, T. J., Mickley, L. J., Jacob, D. J., Ge, C., Wang, J., Payer Sulprizio, M., Croft, B., Ridley, D. A., McConnell, J. R., Sharma, S., Husain, L., Dutkiewicz, V. A., Eleftheriadis, K., Skov, H., and Hopke, P. K.: Multidecadal trends in aerosol

https://doi.org/10.5194/egusphere-2026-4229
Preprint. Discussion started: 28 July 2026

radiative forcing over the Arctic: Contribution of changes in anthropogenic aerosol to Arctic warming since 1980, J. Geophys. Res. Atmospheres, 122, 3573–3594, https://doi.org/10.1002/2016JD025321, 2017.

Buehner, M., McTaggart-Cowan, R., Beaulne, A., Charette, C., Garand, L., Heilliette, S., Lapalme, E., Laroche, S., Macpherson, S. R., Morneau, J., and Zadra, A.: Implementation of Deterministic Weather Forecasting Systems Based on Ensemble–Variational Data Assimilation at Environment Canada. Part I: The Global System, Mon. Weather Rev., 143, 2532–2559, https://doi.org/10.1175/MWR-D-14-00354.1, 2015.

Burrows, S. M., McCluskey, C. S., Cornwell, G., Steinke, I., Zhang, K., Zhao, B., Zawadowicz, M., Raman, A., Kulkarni, G., China, S., Zelenyuk, A., and DeMott, P. J.: Ice-Nucleating Particles That Impact Clouds and Climate: Observational and Modeling Research Needs, Rev. Geophys., 60, e2021RG000745, https://doi.org/10.1029/2021RG000745, 2022.

Casati, B., Robinson, T., Lemay, F., Køltzow, M., Haiden, T., Mekis, E., Lespinas, F., Fortin, V., Gascon, G., Milbrandt, J., and Smith, G.: Performance of the Canadian Arctic Prediction System during the YOPP Special Observing Periods, Atmosphere-Ocean, 61, 246–272, https://doi.org/10.1080/07055900.2023.2191831, 2023.

Chin, M., Ginoux, P., Kinne, S., Torres, O., Holben, B. N., Duncan, B. N., Martin, R. V., Logan, J. A., Higurashi, A., and Nakajima, T.: Tropospheric Aerosol Optical Thickness from the GOCART Model and Comparisons with Satellite and Sun Photometer Measurements, J. Atmospheric Sci., 59, 461–483, https://doi.org/10.1175/1520-0469(2002)059<0461:TAOTFT>2.0.CO;2, 2002.

Cholette, M., Morrison, H., Milbrandt, J. A., and Thériault, J. M.: Parameterization of the Bulk Liquid Fraction on Mixed-Phase Particles in the Predicted Particle Properties (P3) Scheme: Description and Idealized Simulations, J. Atmospheric Sci., 76, 561–582, https://doi.org/10.1175/JAS-D-18-0278.1, 2019.

Cholette, M., Milbrandt, J. A., Morrison, H., Paquin-Ricard, D., and Jacques, D.: Combining Triple-Moment Ice With Prognostic Liquid Fraction in the P3 Microphysics Scheme: Impacts on a Simulated Squall Line, J. Adv. Model. Earth Syst., 15, e2022MS003328, https://doi.org/10.1029/2022MS003328, 2023.

Cholette, M., Milbrandt, J. A., Morrison, H., Kirk, S., and Lalonde, L.-É.: Secondary Ice Production Improves Simulations of Freezing Rain, Geophys. Res. Lett., 51, e2024GL108490, https://doi.org/10.1029/2024GL108490, 2024.

Cober, S. G. and Isaac, G. A.: Characterization of Aircraft Icing Environments with Supercooled Large Drops for Application to Commercial Aircraft Certification, J. Appl. Meteorol. Climatol., 51, 265–284, https://doi.org/10.1175/JAMC-D-11-022.1, 2012.

Cober, S. G., Isaac, G. A., and Strapp, J. W.: Characterizations of Aircraft Icing Environments that Include Supercooled Large Drops, J. Appl. Meteorol., 40, 1984–2002, https://doi.org/10.1175/1520-0450(2001)040<1984:COAIET>2.0.CO;2, 2001.

Colarco, P., Silva, A., Chin, M., and Diehl, T.: Online simulations of global aerosol distributions in the NASA GEOS-4 model and comparisons to satellite and ground-based aerosol optical depth, J. Geophys. Res. Atmospheres, 115, https://doi.org/10.1029/2009JD012820, 2010.

Collins, W. J., Lamarque, J.-F., Schulz, M., Boucher, O., Eyring, V., Hegglin, M. I., Maycock, A., Myhre, G., Prather, M., Shindell, D., and Smith, S. J.: AerChemMIP: quantifying the effects of chemistry and aerosols in CMIP6, Geosci. Model Dev., 10, 585–607, https://doi.org/10.5194/gmd-10-585-2017, 2017.

Cooper, W. A.: Ice Initiation in Natural Clouds, in: Precipitation Enhancement—A Scientific Challenge, American Meteorological Society, Boston, MA, 29–32, https://doi.org/10.1007/978-1-935704-17-1_4, 1986.

https://doi.org/10.5194/egusphere-2026-4229
Preprint. Discussion started: 28 July 2026

Côté, J., Gravel, S., Méthot, A., Patoine, A., Roch, M., and Staniforth, A.: The Operational CMC–MRB Global Environmental Multiscale (GEM) Model. Part I: Design Considerations and Formulation, Mon. Weather Rev., 126, 1373–1395, https://doi.org/10.1175/1520-0493(1998)126<1373:TOCMGE>2.0.CO;2, 1998.

DeMott, P. J., Prenni, A. J., Liu, X., Kreidenweis, S. M., Petters, M. D., Twohy, C. H., Richardson, M. S., Eidhammer, T., and Rogers, D. C.: Predicting global atmospheric ice nuclei distributions and their impacts on climate, Proc. Natl. Acad. Sci., 107, 11217–11222, https://doi.org/10.1073/pnas.0910818107, 2010.

Dengate, J., Takeishi, A., and Rosky, E.: Sensitivity Tests of the P3 Microphysical Scheme: Modifying Ice Fall Speeds in CM1, 2025.

Dietlicher, R., Neubauer, D., and Lohmann, U.: Prognostic parameterization of cloud ice with a single category in the aerosol-climate model ECHAM(v6.3.0)-HAM(v2.3), Geosci Model Dev, 11, 1557–1576, https://doi.org/10.5194/gmd-11-1557-2018, 2018.

Eisinger, M., Marnas, F., Wallace, K., Kubota, T., Tomiyama, N., Ohno, Y., Tanaka, T., Tomita, E., Wehr, T., and Bernaerts, D.: The EarthCARE mission: science data processing chain overview, Atmospheric Meas. Tech., 17, 839–862, https://doi.org/10.5194/amt-17-839-2024, 2024.

Fan, J., Wang, Y., Rosenfeld, D., and Liu, X.: Review of Aerosol–Cloud Interactions: Mechanisms, Significance, and Challenges, J. Atmospheric Sci., 73, 4221–4252, https://doi.org/10.1175/JAS-D-16-0037.1, 2016.

Fan, J., Rosenfeld, D., Zhang, Y., Giangrande, S. E., Li, Z., Machado, L. A. T., Martin, S. T., Yang, Y., Wang, J., Artaxo, P., Barbosa, H. M. J., Braga, R. C., Comstock, J. M., Feng, Z., Gao, W., Gomes, H. B., Mei, F., Pöhlker, C., Pöhlker, M. L., Pöschl, U., and de Souza, R. A. F.: Substantial convection and precipitation enhancements by ultrafine aerosol particles, Science, 359, 411–418, https://doi.org/10.1126/science.aan8461, 2018.

Forbes, R. M. and Ahlgrimm, M.: On the Representation of High-Latitude Boundary Layer Mixed-Phase Cloud in the ECMWF Global Model, Mon. Weather Rev., 142, 3425–3445, https://doi.org/10.1175/MWR-D-13-00325.1, 2014.

Fu, S. and Xue, H.: The Effect of Ice Nuclei Efficiency on Arctic Mixed-Phase Clouds from Large-Eddy Simulations, J. Atmospheric Sci., 74, 3901–3913, https://doi.org/10.1175/JAS-D-17-0112.1, 2017.

Ghosh, P., Evans, K. J., Grosvenor, D. P., Kang, H.-G., Mahajan, S., Xu, M., Zhang, W., and Gordon, H.: Assessing modifications to the Abdul-Razzak and Ghan aerosol activation parameterization (version ARG2000) to improve simulated aerosol–cloud radiative effects in the UK Met Office Unified Model (UM version 13.0), Geosci. Model Dev., 18, 4899–4913, https://doi.org/10.5194/gmd-18-4899-2025, 2025.

Ginoux, P., Chin, M., Tegen, I., Prospero, J. M., Holben, B., Dubovik, O., and Lin, S.-J.: Sources and distributions of dust aerosols simulated with the GOCART model, J. Geophys. Res. Atmospheres, 106, 20255–20273, https://doi.org/10.1029/2000JD000053, 2001.

Girard, C., Plante, A., Desgagné, M., McTaggart-Cowan, R., Côté, J., Charron, M., Gravel, S., Lee, V., Patoine, A., Qaddouri, A., Roch, M., Spacek, L., Tanguay, M., Vaillancourt, P. A., and Zadra, A.: Staggered Vertical Discretization of the Canadian Environmental Multiscale (GEM) Model Using a Coordinate of the Log-Hydrostatic-Pressure Type, Mon. Weather Rev., 142, 1183–1196, https://doi.org/10.1175/MWR-D-13-00255.1, 2014.

Gjelsvik, A. B., David, R. O., Carlsen, T., Hellmuth, F., Hofer, S., McGraw, Z., Sodemann, H., and Storelvmo, T.: Using a region-specific ice-nucleating particle parameterization improves the representation of Arctic clouds in a global climate model, Atmospheric Chem. Phys., 25, 1617–1637, https://doi.org/10.5194/acp-25-1617-2025, 2025.

https://doi.org/10.5194/egusphere-2026-4229
Preprint. Discussion started: 28 July 2026

Glassmeier, F., Possner, A., Vogel, B., Vogel, H., and Lohmann, U.: A comparison of two chemistry and aerosol schemes on the regional scale and the resulting impact on radiative properties and liquid- and ice-phase aerosol–cloud interactions, Atmospheric Chem. Phys., 17, 8651–8680, https://doi.org/10.5194/acp-17-8651-2017, 2017.

Gramlich, Y., Siegel, K., Haslett, S. L., Cremer, R. S., Lunder, C., Kommula, S. M., Buchholz, A., Yttri, K. E., Chen, G., Krejci, R., Zieger, P., Virtanen, A., Riipinen, I., and Mohr, C.: Impact of Biomass Burning on Arctic Aerosol Composition, ACS Earth Space Chem., 8, 920–936, https://doi.org/10.1021/acsearthspacechem.3c00187, 2024.

Grell, G. A., Peckham, S. E., Schmitz, R., McKeen, S. A., Frost, G., Skamarock, W. C., and Eder, B.: Fully coupled "online" chemistry within the WRF model, Atmos. Environ., 39, 6957–6975, https://doi.org/10.1016/j.atmosenv.2005.04.027, 2005.

Hallett, J. and Mossop, S. C.: Production of secondary ice particles during the riming process, Nature, 249, 26–28, https://doi.org/10.1038/249026a0, 1974.

Hudson, J. G.: Cloud Condensation Nuclei, J. Appl. Meteorol. Climatol., 32, 596–607, https://doi.org/10.1175/1520-0450(1993)032<0596:CCN>2.0.CO;2, 1993.

Illingworth, A. J., Barker, H. W., Beljaars, A., Ceccaldi, M., Chepfer, H., Clerbaux, N., Cole, J., Delanoë, J., Domenech, C., Donovan, D. P., Fukuda, S., Hirakata, M., Hogan, R. J., Huenerbein, A., Kollias, P., Kubota, T., Nakajima, T., Nakajima, T. Y., Nishizawa, T., Ohno, Y., Okamoto, H., Oki, R., Sato, K., Satoh, M., Shephard, M. W., Velázquez-Blázquez, A., Wandinger, U., Wehr, T., and Zadelhoff, G.-J. van: The EarthCARE Satellite: The Next Step Forward in Global Measurements of Clouds, Aerosols, Precipitation, and Radiation, Bull. Am. Meteorol. Soc., 96, 1311–1332, https://doi.org/10.1175/BAMS-D-12-00227.1, 2015.

James, E. P., Alexander, C. R., Dowell, D. C., Weygandt, S. S., Benjamin, S. G., Manikin, G. S., Brown, J. M., Olson, J. B., Hu, M., Smirnova, T. G., Ladwig, T., Kenyon, J. S., and Turner, D. D.: The High-Resolution Rapid Refresh (HRRR): An Hourly Updating Convection-Allowing Forecast Model. Part II: Forecast Performance, Weather Forecast., 37, 1397–1417, https://doi.org/10.1175/WAF-D-21-0130.1, 2022.

Jian, B., Ma, Z., Liu, Q., Li, Z., Deng, L., Nie, H., Liu, C., Zhao, C., Sun, J., and Shen, X.: An advanced double-moment cloud microphysics scheme with explicit aerosol-cloud interactions and its performance in quantitative precipitation forecasting (QPF) in the CMA-MESO V5.0, Atmospheric Res., 331, 108649, https://doi.org/10.1016/j.atmosres.2025.108649, 2026.

Jiang, M., Feng, J., Li, Z., Sun, R., Hou, Y.-T., Zhu, Y., Wan, B., Guo, J., and Cribb, M.: Potential influences of neglecting aerosol effects on the NCEP GFS precipitation forecast, Atmospheric Chem. Phys., 17, 13967–13982, https://doi.org/10.5194/acp-17-13967-2017, 2017.

Kain, J. S. and Fritsch, J. M.: A One-Dimensional Entraining/Detraining Plume Model and Its Application in Convective Parameterization, J. Atmospheric Sci., 47, 2784–2802, https://doi.org/10.1175/1520-0469(1990)047<2784:AODEPM>2.0.CO;2, 1990.

Kain, J. S. and Fritsch, J. M.: Convective Parameterization for Mesoscale Models: The Kain-Fritsch Scheme, in: The Representation of Cumulus Convection in Numerical Models, edited by: Emanuel, K. A. and Raymond, D. J., American Meteorological Society, Boston, MA, 165–170, https://doi.org/10.1007/978-1-935704-13-3_16, 1993.

Kanji, Z. A., Ladino, L. A., Wex, H., Boose, Y., Burkert-Kohn, M., Cziczo, D. J., and Krämer, M.: Overview of Ice Nucleating Particles, Meteorol. Monogr., 58, 1.1-1.33, https://doi.org/10.1175/AMSMONOGRAPHS-D-16-0006.1, 2017.

https://doi.org/10.5194/egusphere-2026-4229
Preprint. Discussion started: 28 July 2026

Khain, A., Rosenfeld, D., and Pokrovsky, A.: Aerosol impact on the dynamics and microphysics of deep convective clouds, Q. J. R. Meteorol. Soc., 131, 2639–2663, https://doi.org/10.1256/qj.04.62, 2005.

Khvorostyanov, V. I. and Curry, J. A.: The Theory of Ice Nucleation by Heterogeneous Freezing of Deliquescent Mixed CCN. Part II: Parcel Model Simulation, J. Atmospheric Sci., 62, 261–285, https://doi.org/10.1175/JAS-3367.1, 2005.

Koop, T., Luo, B., Tsias, A., and Peter, T.: Water activity as the determinant for homogeneous ice nucleation in aqueous solutions, Nature, 406, 611–614, https://doi.org/10.1038/35020537, 2000.

Korolev, A.: Limitations of the Wegener–Bergeron–Findeisen Mechanism in the Evolution of Mixed-Phase Clouds, J. Atmospheric Sci., 64, 3372–3375, https://doi.org/10.1175/JAS4035.1, 2007.

Korolev, A. and Milbrandt, J.: How Are Mixed-Phase Clouds Mixed?, Geophys. Res. Lett., 49, e2022GL099578, https://doi.org/10.1029/2022GL099578, 2022.

Korolev, A. V.: Rates of phase transformations in mixed-phase clouds, Q. J. R. Meteorol. Soc., 134, 595–608, https://doi.org/10.1002/qj.230, 2008.

Kuo, K.-T., Kuo, Y.-H., Neelin, J. D., and Wu, C.-M.: Deep convection despite strong surface inhibition-examples with cloud-resolving and anelastic convective entity models, ESS Open Arch., 2026, https://doi.org/10.22541/essoar.175760544.45647014/v2, 2026.

Lamarque, J.-F., Shindell, D. T., Josse, B., Young, P. J., Cionni, I., Eyring, V., Bergmann, D., Cameron-Smith, P., Collins, W. J., Doherty, R., Dalsoren, S., Faluvegi, G., Folberth, G., Ghan, S. J., Horowitz, L. W., Lee, Y. H., MacKenzie, I. A., Nagashima, T., Naik, V., Plummer, D., Righi, M., Rumbold, S. T., Schulz, M., Skeie, R. B., Stevenson, D. S., Strode, S., Sudo, K., Szopa, S., Voulgarakis, A., and Zeng, G.: The Atmospheric Chemistry and Climate Model Intercomparison Project (ACCMIP): overview and description of models, simulations and climate diagnostics, Geosci. Model Dev., 6, 179–206, https://doi.org/10.5194/gmd-6-179-2013, 2013.

Langille, J., Rieger, L. A., Blanchard, Y., Blanchet, J.-P., Bourassa, A., Degenstein, D., Huang, Y., Strong, K., Walker, K., Zawada, D., Braun, S., Cole, J., Mariani, Z., Mclinden, C., Paquin-Ricard, D., Sioris, C., Qu, Z., Wolde, M., Wang, X., Al-Abadleh, H. A., Ariya, P., Beltrami, H., Chang, R., Fletcher, C. G., Goldblatt, C., Grenier, P., Gyakum, J., Kushner, P., Luca, A. D., MacDougall, A. H., O'Neill, N., Pausata, F. S. R., Sica, R., Tan, I., Thériault, J. M., Tegtmeier, S., Toohey, M., Ward, W., and Wiacek, A.: The High-Altitude Aerosols, Water Vapor, and Clouds Mission: Concept, Scientific Objectives, and Data Products, Bull. Am. Meteorol. Soc., 106, E2358–E2383, https://doi.org/10.1175/BAMS-D-23-0309.1, 2025.

Li, J. and Barker, H. W.: A Radiation Algorithm with Correlated-k Distribution. Part I: Local Thermal Equilibrium, J. Atmospheric Sci., 62, 286–309, https://doi.org/10.1175/JAS-3396.1, 2005.

Li, Z., Wang, Y., Guo, J., Zhao, C., Cribb, M. C., Dong, X., Fan, J., Gong, D., Huang, J., Jiang, M., Jiang, Y., Lee, S.-S., Li, H., Li, J., Liu, J., Qian, Y., Rosenfeld, D., Shan, S., Sun, Y., Wang, H., Xin, J., Yan, X., Yang, X., Yang, X., Zhang, F., and Zheng, Y.: East Asian Study of Tropospheric Aerosols and their Impact on Regional Clouds, Precipitation, and Climate (EAST-AIRCPC), J. Geophys. Res. Atmospheres, 124, 13026–13054, https://doi.org/10.1029/2019JD030758, 2019.

Lohmann, U.: Aerosol Effects on Clouds and Climate, Space Sci. Rev., 125, 129–137, https://doi.org/10.1007/s11214-006-9051-8, 2006.

Mariani, Z., Huang, L., Crawford, R., Blanchet, J.-P., Hicks-Jalali, S., Mekis, E., Pelletier, L., Rodriguez, P., and Strawbridge, K.: Enhanced automated meteorological observations at the Canadian Arctic Weather Science (CAWS) supersites, Earth Syst. Sci. Data, 14, 4995–5017, https://doi.org/10.5194/essd-14-4995-2022, 2022.

Mariani, Z., Morris, S. M., Uttal, T., Akish, E., Crawford, R., Huang, L., Day, J., Tjernström, J., Godøy, Ø., Ferrighi, L., Hartten, L. M., Holt, J., Cox, C. J., O'Connor, E., Pirazzini, R., Maturilli, M., Prakash, G., Mather, J., Strong, K., Fogal, P., Kustov, V., Svensson, G., Gallagher, M., and Vasel, B.: Special Observing Period (SOP) data for the Year of Polar Prediction site Model Intercomparison Project (YOPPsiteMIP), Earth Syst. Sci. Data, 16, 3083–3124, https://doi.org/10.5194/essd-16-3083-2024, 2024.

Milbrandt, J. A. and Morrison, H.: Parameterization of Cloud Microphysics Based on the Prediction of Bulk Ice Particle Properties. Part III: Introduction of Multiple Free Categories, J. Atmospheric Sci., 73, 975–995, https://doi.org/10.1175/JAS-D-15-0204.1, 2016.

Milbrandt, J. A., Bélair, S., Faucher, M., Vallée, M., Carrera, M. L., and Glazer, A.: The Pan-Canadian High Resolution (2.5 km) Deterministic Prediction System, Weather Forecast., 31, 1791–1816, https://doi.org/10.1175/WAF-D-16-0035.1, 2016.

Milbrandt, J. A., Morrison, H., II, D. T. D., and Paukert, M.: A Triple-Moment Representation of Ice in the Predicted Particle Properties (P3) Microphysics Scheme, J. Atmospheric Sci., 78, 439–458, https://doi.org/10.1175/JAS-D-20-0084.1, 2021.

Moran, M. D., Savic-Jovcic, V., Stroud, C. A., Ménard, S., Gong, W., Zhang, J., Zheng, Q., Chen, J., Akingunola, A., Lupu, A., Menelaou, K., and Munoz-Alpizar, R.: Operational chemical weather forecasting with the ECCC online Regional Air Quality Deterministic Prediction System version 023 (RAQDPS023) – Part 1: System description, EGUsphere, 2025, 1–99, https://doi.org/10.5194/egusphere-2025-4323, 2025.

Morrison, H. and Milbrandt, J. A.: Parameterization of Cloud Microphysics Based on the Prediction of Bulk Ice Particle Properties. Part I: Scheme Description and Idealized Tests, J. Atmospheric Sci., 72, 287–311, https://doi.org/10.1175/JAS-D-14-0065.1, 2015.

Morrison, H. and Pinto, J. O.: Mesoscale Modeling of Springtime Arctic Mixed-Phase Stratiform Clouds Using a New Two-Moment Bulk Microphysics Scheme, J. Atmospheric Sci., 62, 3683–3704, https://doi.org/10.1175/JAS3564.1, 2005.

Morrison, H. and Pinto, J. O.: Intercomparison of Bulk Cloud Microphysics Schemes in Mesoscale Simulations of Springtime Arctic Mixed-Phase Stratiform Clouds, Mon. Weather Rev., 134, 1880–1900, https://doi.org/10.1175/MWR3154.1, 2006.

Morrison, H., de Boer, G., Feingold, G., Harrington, J., Shupe, M. D., and Sulia, K.: Resilience of persistent Arctic mixed-phase clouds, Nat. Geosci., 5, 11–17, https://doi.org/10.1038/ngeo1332, 2012.

Morrison, H., Milbrandt, J. A., Bryan, G. H., Ikeda, K., Tessendorf, S. A., and Thompson, G.: Parameterization of Cloud Microphysics Based on the Prediction of Bulk Ice Particle Properties. Part II: Case Study Comparisons with Observations and Other Schemes, J. Atmospheric Sci., 72, 312–339, https://doi.org/10.1175/JAS-D-14-0066.1, 2015.

Morrison, H., van Lier-Walqui, M., Fridlind, A. M., Grabowski, W. W., Harrington, J. Y., Hoose, C., Korolev, A., Kumjian, M. R., Milbrandt, J. A., Pawlowska, H., Posselt, D. J., Prat, O. P., Reimel, K. J., Shima, S.-I., van Diedenhoven, B., and Xue, L.: Confronting the Challenge of Modeling Cloud and Precipitation Microphysics, J. Adv. Model. Earth Syst., 12, e2019MS001689, https://doi.org/10.1029/2019MS001689, 2020.

Morrison, H., Milbrandt, J. A., and Cholette, M.: A Complete Three-Moment Representation of Ice in the Predicted Particle Properties (P3) Microphysics Scheme, J. Adv. Model. Earth Syst., 17, e2024MS004644, https://doi.org/10.1029/2024MS004644, 2025.

https://doi.org/10.5194/egusphere-2026-4229
Preprint. Discussion started: 28 July 2026

Murray, B. J., O'Sullivan, D., Atkinson, J. D., and Webb, M. E.: Ice nucleation by particles immersed in supercooled cloud droplets, Chem Soc Rev, 41, 6519–6554, https://doi.org/10.1039/C2CS35200A, 2012.

Norgren, M. S., de Boer, G., and Shupe, M. D.: Observed aerosol suppression of cloud ice in low-level Arctic mixed-phase clouds, Atmospheric Chem. Phys., 18, 13345–13361, https://doi.org/10.5194/acp-18-13345-2018, 2018.

Papaevangelou, N., Villanueva, D., Eirund, G. K., Chen, J., Dedekind, Z., and Lohmann, U.: Simulations of Selective Seeding of Hailstorms—A Summertime Case Study over Switzerland, J. Appl. Meteorol. Climatol., 64, 1509–1524, https://doi.org/10.1175/JAMC-D-24-0121.1, 2025.

Paukert, M. and Hoose, C.: Modeling immersion freezing with aerosol-dependent prognostic ice nuclei in Arctic mixed-phase clouds, J. Geophys. Res. Atmospheres, 119, 9073–9092, https://doi.org/10.1002/2014JD021917, 2014.

Ramanathan, V., Crutzen, P. J., Kiehl, J. T., and Rosenfeld, D.: Aerosols, Climate, and the Hydrological Cycle, Science, 294, 2119–2124, https://www.science.org/doi/abs/10.1126/science.1064034, 2001.

Rasmussen, R., Wade, C., Hage, F., Landolt, S., Tryhane, M., Cole, J., Ramsay, A., Fleming, D., Moore, R. K., Davis, A., Reis, B., Lisi, T., Kjolleberg, M., and Rosenlund, K. M.: New Ground Deicing Hazard Associated with Freezing Drizzle Ingestion by Jet Engines, J. Aircr., 43, 1448–1457, https://doi.org/10.2514/1.20799, 2006.

Rémy, S., Kipling, Z., Flemming, J., Boucher, O., Nabat, P., Michou, M., Bozzo, A., Ades, M., Huijnen, V., Benedetti, A., Engelen, R., Peuch, V.-H., and Morcrette, J.-J.: Description and evaluation of the tropospheric aerosol scheme in the European Centre for Medium-Range Weather Forecasts (ECMWF) Integrated Forecasting System (IFS-AER, cycle 45R1), Geosci. Model Dev., 12, 4627–4659, https://doi.org/10.5194/gmd-12-4627-2019, 2019.

Rosenfeld, D.: Aerosol-Cloud Interactions Control of Earth Radiation and Latent Heat Release Budgets, Space Sci. Rev., 125, 149–157, https://doi.org/10.1007/s11214-006-9053-6, 2006.

Rosenfeld, D., Lohmann, U., Raga, G. B., O'Dowd, C. D., Kulmala, M., Fuzzi, S., Reissell, A., and Andreae, M. O.: Flood or Drought: How Do Aerosols Affect Precipitation?, Science, 321, 1309–1313, https://doi.org/10.1126/science.1160606, 2008.

Rosenfeld, D., Andreae, M. O., Asmi, A., Chin, M., de Leeuw, G., Donovan, D. P., Kahn, R., Kinne, S., Kivekäs, N., Kulmala, M., Lau, W., Schmidt, K. S., Suni, T., Wagner, T., Wild, M., and Quaas, J.: Global observations of aerosol-cloud-precipitation-climate interactions, Rev. Geophys., 52, 750–808, https://doi.org/10.1002/2013RG000441, 2014.

Ross, T. I. D. and Lasher-Trapp, S.: Investigating the Relative Roles of INPs and CCN in a Simulated Thunderstorm Using a New Immersion Freezing Algorithm, J. Geophys. Res. Atmospheres, 130, e2024JD042592, https://doi.org/10.1029/2024JD042592, 2025.

Sauerland, F., Souverijns, N., Possner, A., Wex, H., Van Overmeiren, P., Mangold, A., Van Weverberg, K., and van Lipzig, N.: Ice-nucleating particle concentration impacts cloud properties over Dronning Maud Land, East Antarctica, in COSMO-CLM^2, Atmospheric Chem. Phys., 24, 13751–13768, https://doi.org/10.5194/acp-24-13751-2024, 2024.

Schäfer, B., David, R. O., Hodnebrog, Ø., and Storelvmo, T.: Response of an Arctic Mixed-Phase Cloud to Ice-Nucleating Particle Perturbations and Warming, Geophys. Res. Lett., 52, e2024GL114467, https://doi.org/10.1029/2024GL114467, 2025.

Seifert, A. and Siewert, C.: An ML-Based P3-Like Multimodal Two-Moment Ice Microphysics in the ICON Model, J. Adv. Model. Earth Syst., 16, e2023MS004206, https://doi.org/10.1029/2023MS004206, 2024.

https://doi.org/10.5194/egusphere-2026-4229
Preprint. Discussion started: 28 July 2026

Shi, Y., Liu, X., Wu, M., Zhao, X., Ke, Z., and Brown, H.: Relative importance of high-latitude local and long-range-transported dust for Arctic ice-nucleating particles and impacts on Arctic mixed-phase clouds, Atmospheric Chem. Phys., 22, 2909–2935, https://doi.org/10.5194/acp-22-2909-2022, 2022.

Slinn, W. G. N. and Shen, S. F.: Anisotropic Brownian diffusion and precipitation scavenging of submicron particles, J. Geophys. Res. 1896-1977, 75, 2267–2270, https://doi.org/10.1029/JC075i012p02267, 1970.

Solomon, A., de Boer, G., Creamean, J. M., McComiskey, A., Shupe, M. D., Maahn, M., and Cox, C.: The relative impact of cloud condensation nuclei and ice nucleating particle concentrations on phase partitioning in Arctic mixed-phase stratocumulus clouds, Atmospheric Chem. Phys., 18, 17047–17059, https://doi.org/10.5194/acp-18-17047-2018, 2018.

Sotiropoulou, G., Ickes, L., Nenes, A., and Ekman, A. M. L.: Ice multiplication from ice–ice collisions in the high Arctic: sensitivity to ice habit, rimed fraction, ice type and uncertainties in the numerical description of the process, Atmospheric Chem. Phys., 21, 9741–9760, https://doi.org/10.5194/acp-21-9741-2021, 2021.

Sundqvist, H., Berge, E., and Kristjánsson, J. E.: Condensation and Cloud Parameterization Studies with a Mesoscale Numerical Weather Prediction Model, Mon. Weather Rev., 117, 1641–1657, https://doi.org/10.1175/1520-0493(1989)117<1641:CACPSW>2.0.CO;2, 1989.

Tan, I., Sotiropoulou, G., Taylor, P. C., Zamora, L., and Wendisch, M.: A Review of the Factors Influencing Arctic Mixed-Phase Clouds: Progress and Outlook, in: Clouds and Their Climatic Impacts, American Geophysical Union (AGU), 103–132, https://doi.org/10.1002/9781119700357.ch5, 2023.

Thompson, G. and Eidhammer, T.: A Study of Aerosol Impacts on Clouds and Precipitation Development in a Large Winter Cyclone, J. Atmospheric Sci., 71, 3636–3658, https://doi.org/10.1175/JAS-D-13-0305.1, 2014.

Tobo, Y., Prenni, A. J., DeMott, P. J., Huffman, J. A., McCluskey, C. S., Tian, G., Pöhlker, C., Pöschl, U., and Kreidenweis, S. M.: Biological aerosol particles as a key determinant of ice nuclei populations in a forest ecosystem, J. Geophys. Res. Atmospheres, 118, 10,100-10,110, https://doi.org/10.1002/jgrd.50801, 2013.

Walters, D., Baran, A. J., Boutle, I., Brooks, M., Earnshaw, P., Edwards, J., Furtado, K., Hill, P., Lock, A., Manners, J., Morcrette, C., Mulcahy, J., Sanchez, C., Smith, C., Stratton, R., Tennant, W., Tomassini, L., Van Weverberg, K., Vosper, S., Willett, M., Browse, J., Bushell, A., Carslaw, K., Dalvi, M., Essery, R., Gedney, N., Hardiman, S., Johnson, B., Johnson, C., Jones, A., Jones, C., Mann, G., Milton, S., Rumbold, H., Sellar, A., Ujiie, M., Whitall, M., Williams, K., and Zerroukat, M.: The Met Office Unified Model Global Atmosphere 7.0/7.1 and JULES Global Land 7.0 configurations, Geosci Model Dev, 12, 1909–1963, https://doi.org/10.5194/gmd-12-1909-2019, 2019.

Wang, J., Fan, J., Feng, Z., Zhang, K., Roesler, E., Hillman, B., Shpund, J., Lin, W., and Xie, S.: Impact of a New Cloud Microphysics Parameterization on the Simulations of Mesoscale Convective Systems in E3SM, J. Adv. Model. Earth Syst., 13, e2021MS002628, https://doi.org/10.1029/2021MS002628, 2021.

Wang, X., Zhang, L., and Moran, M. D.: Uncertainty assessment of current size-resolved parameterizations for below-cloud particle scavenging by rain, Atmospheric Chem. Phys., 10, 5685–5705, https://doi.org/10.5194/acp-10-5685-2010, 2010.

Wang, Y., Li, Z., Zhang, Y., Du, W., Zhang, F., Tan, H., Xu, H., Fan, T., Jin, X., Fan, X., Dong, Z., Wang, Q., and Sun, Y.: Characterization of aerosol hygroscopicity, mixing state, and CCN activity at a suburban site in the central North China Plain, Atmospheric Chem. Phys., 18, 11739–11752, https://doi.org/10.5194/acp-18-11739-2018, 2018.

https://doi.org/10.5194/egusphere-2026-4229
Preprint. Discussion started: 28 July 2026

Wehr, T., Kubota, T., Tzeremes, G., Wallace, K., Nakatsuka, H., Ohno, Y., Koopman, R., Rusli, S., Kikuchi, M., Eisinger, M., Tanaka, T., Taga, M., Deghaye, P., Tomita, E., and Bernaerts, D.: The EarthCARE mission – science and system overview, Atmospheric Meas. Tech., 16, 3581–3608, https://doi.org/10.5194/amt-16-3581-2023, 2023.

Xie, S., Liu, X., Zhao, C., and Zhang, Y.: Sensitivity of CAM5-Simulated Arctic Clouds and Radiation to Ice Nucleation Parameterization, J. Clim., 26, 5981–5999, https://doi.org/10.1175/JCLI-D-12-00517.1, 2013.

Yu, L., Zhang, M., Wang, L., Li, H., and Li, J.: Characteristics of Aerosols and Clouds and Their Role in Earth's Energy Budget, J. Clim., 37, 995–1014, https://doi.org/10.1175/JCLI-D-23-0414.1, 2024.

Zhao, C., Lin, Y., Wu, F., Wang, Y., Li, Z., Rosenfeld, D., and Wang, Y.: Enlarging Rainfall Area of Tropical Cyclones by Atmospheric Aerosols, Geophys. Res. Lett., 45, 8604–8611, https://doi.org/10.1029/2018GL079427, 2018.

Zhao, X. and Liu, X.: Primary and secondary ice production: interactions and their relative importance, Atmospheric Chem. Phys., 22, 2585–2600, https://doi.org/10.5194/acp-22-2585-2022, 2022.

Zhou, C., Zhang, X., Gong, S., Wang, Y., and Xue, M.: Improving aerosol interaction with clouds and precipitation in a regional chemical weather modeling system, Atmospheric Chem. Phys., 16, 145–160, https://doi.org/10.5194/acp-16-145-2016, 2016.

Dataset:

Cholette, M. (2026). Introduction of prognostic aerosols in the P3 microphysics scheme v6.0: Simulation of layered Arctic mixed-phase clouds. https://doi.org/10.5281/zenodo.21169210

NOAA Geostationary Operational Environmental Satellites (GOES) 16, 17, 18 & 19 was accessed on 22 May 2026 from https://registry.opendata.aws/noaa-goes.